SIMULATION AND APPLICATION OF LIGHT SCATTERING PROPERTIES FOR SCATTERERS WITH LARGE ASPECT RATIOS

A Dissertation

by

BINGQIANG SUN

Submitted to the Office of Graduate and Professional Studies of
Texas A&M University
in partial fulfillment of the requirements for the degree of

DOCTOR OF PHILOSOPHY

Chair of Committee,	George W. Kattawar
Co-Chair of Committee,	Ping Yang
Committee Members,	Edward S. Fry
	Alexei V. Sokolov
Head of Department,	George R. Welch

December 2014

Major Subject: Physics

ABSTRACT

For scatterers with axial or N-fold rotational symmetry, the T-matrix is one of the most efficient techniques to obtain the scattering properties. Extended boundary condition method (EBCM) and invariant imbedding T-matrix method (II-TM) are currently two of the most effective realizations of the T-matrix. The T-matrix of the scatterers with the rotational symmetry will be fully or partially decoupled between different azimuthal components, which can dramatically increase calculation efficiencies.

However, the ill-conditioned problem will occur for the EBCM whereas memory requirements and time consumption will be exponentially increased for the II-TM when scatterers have large aspect ratios (the ratios of the heights to the characteristic widths of the scatterers). The many-body iterative T-matrix method (MBIT), which uses the T-matrix and many-body techniques, is developed and generalized to target the homogeneous and inhomogeneous scatterers with large aspect ratios.

For infinite scatterers with one dimension periodicity, a semi-analytical solution instead of the iterative technique has been obtained by extending the application of the MBIT method to infinite number of sub-units. The semi-analytical solution of a scatterer with 1-D periodicity can be treated as an proxy and the limit of the corresponding finite scatterer with extreme large aspect ratios. For oceanic diatom scatterers, which have chain structures in preferential orientations, the MBIT method is applied to get the scattering properties, which can be the indicators of scatterer orientations, compositions, and shapes.

DEDICATION

To my family

ACKNOWLEDGEMENTS

First, I would like to thank my advisors, Dr. George W. Kattawar and Dr. Ping Yang. They are great scientiests, with enthusiasms and inspiration to science and great advisors always with patient and insight to my researches. In the almost past five years, I have learned a lot on how to be a good researcher from them, which definitely will affect my future research life. I would like to thank my committee members, Dr. Edward S. Fry and Dr. Alexei V. Sokolov. Their comments and suggestions on my researches are very helpful. Also, thank Dr. David M. Lee for attending my prelim exam.

I would like to give my special thanks to Drs. Lei Be, Meng Gao and Yang Du. Working with them is an enjoying experience, always learning new knowledge from them. Meng is also a good badminton player. In our badminton-playing time, Meng is a spontaneous leader. Dr. Yang Du gave me a lot of help and guidance on my research during his visiting time to our group. Part of the credit of my research should be given to him. Also thanks group members, Yu You, Dong Sun, Xin Huang, Chenxi Wang, Bingqi Yi, Chao Liu, Dayou Chen, Jianping Liu, Angela Marotta, and all others from Dr. Kattawar and Dr. Yang's groups. It is a memorable experience to work with them.

I would like to thank my friends, Bin Yang, Ruiyuan Liu, Zhongwei Sun, Zilong Chang, Keke Zheng, Yi Cui and all others. Communication with them makes the living in the small town full of variety.

I would like to thank my wife, my parents and my sister. They always support and accompany me to get through the whole process. Also thanks my son, whose birth brings more happiness into my family.

TABLE OF CONTENTS

Page

LIST OF FIGURES

FIGURE Page

1. INTRODUCTION*

In the simulation of light scattering, the T-matrix method is a powerful technique to get the scattering properties of a single scatterer, especially one with axial or N-fold rotational symmetry [1, 2, 3]. Extended boundary condition method (EBCM) [4, 5] and invariant imbedding T-matrix method (II-TM) [6, 7] are two of the most effective realizations for the T-matrix method. However, the effectiveness of T-matrix method will be highly reduced with the increase of aspect ratio of a scatterer. The matrix inversion process will bring ill-condition problems for EBCM whereas the time consumption and memory requirements during calculations will increase dramatically for II-TM.

Based on T-matrix and many-body techniques, a many-body iterative T-matrix method (MBIT) was developed to target scatterers with large aspect ratios [8, 9]. The aspect ratio is defined as the ratio of the height and the characteristic length of the cross-section of a scatterer. It is theoretically proven that, by dividing a scatterer with a large aspect ratio into several sub-units with small aspect ratios along the direction of the height, its scattering properties can be iteratively obtained in terms of those of the sub-units. The stabilized bi-conjugate gradient iterative method has been employed to accelerate the convergence rate [10, 11, 12]. The axial translational coefficients are employed to take the different frame of references the sub-units have been using into consideration [13, 14, 15, 16]. The method has been generalized from homogeneous to inhomogeneous scatterers with large aspect ratios. Using on the T-matrix of the sub-unit, the MBIT method has been applied to various prolate

*Figure 1.1 is reprinted with permission from "Atmospheric ice crystals over the antarctic plateau in winter" by V. P. Walden, S. G. Warren and E. Tuttle, 2003. J. Appl. Meteorol., **42**(10), 1391-1405. Copyright 2003 @American Meteorological Society.

scatterers with or without axial symmetry, such as, cylinders, spheroids, prisms based on different orders of equilateral polygons, or combined shapes [8, 9].

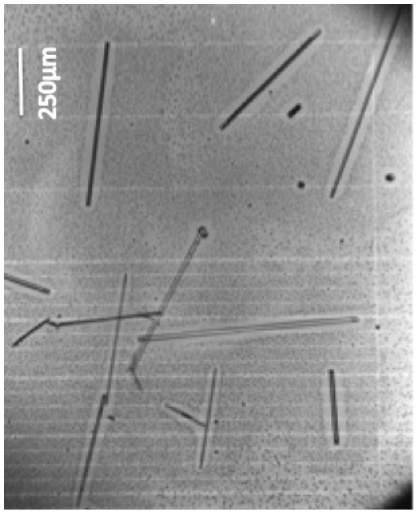

Figure 1.1: Long prism crystals (From Walden et al. [17]).

In atmospheric observations, there are a lot of scatterers with extremely large aspect ratios [17]. Figure 1.1 shows the long prism Shimizu crystals and the scribe is $250\mu m$ apart [17]. In this case, the scattering properties of the scatterers can be compared with those of the corresponding infinite scatterers with one dimensional periodicity, which are obtained by extending their two ends to the infinity. The MBIT method is correspondingly extended to simulate the scattering properties of a scatterer with one dimensional periodicity [18]. A semi-analytical solution is obtained in terms of the T-matrix of a sub-unit and the axial translational coefficients [13, 14, 15, 16]. A direct matrix inversion is employed instead of an iterative method. Relative to numerically accurate methods, such as discrete dipole approximation method [19] and finite difference time domain method [20], the semi-

analytical solution can be computationally efficient. Moreover, the solution of 1-D periodic scatterer can be treated as the proxy of the corresponding scatterer with the same cross-section but extremely large aspect ratios [18].

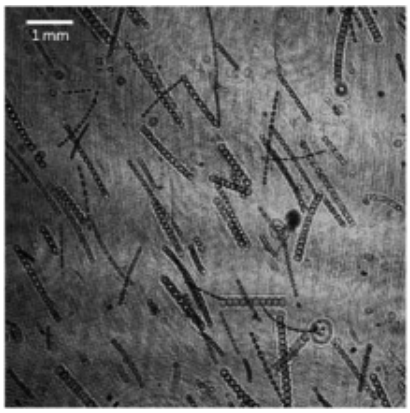

Figure 1.2: Diatom chains.

A lot of oceanic observations show that the marine scatterers, such as, diatoms, not only have large aspect ratios, but also connect together to form diatom chains. Figure 1.2 shows the diatom chains within a phytoplankton thin layer in East Sound, WA, 2013 using the HOLOCAM symtem [21]. These diatom chains are essentially horizontally oriented due to current flow. Moreover, these diatom chains have some specific compositions and shapes in the ocean. The MBIT method can be properly applied to study the scattering properties of these diatom chains. The scattering patterns can be the indicators to detect orientations, compositions, and shapes. The refractive indices of diatoms relative to water are close unity. These particles are so-called soft particles, whose forward scattering is dominated by the anomalous diffraction [22], which contains the inference between diffraction and direct transmission, instead of the diffraction. The diffraction is dependent on the shape and

independent of the refractive index of a scatterer.

2. LIGHT SCATTERING BY A SINGLE SCATTERER AND T-MATRIX METHOD

2.1 Scattering by a single scatterer

Light scattering by a single scatterer is the foundation of remote sensing from active and passive sources as well as its use in radiative transfer theory. There are many ways to describe light scattering. The commonly used one is based on the scattering plane, which contains the incident and scattered directions [22].

The incident wave is assumed to be a plane wave since any field can be decomposed into superpositions of plane waves in terms of a Fourier transformation:

$$\mathbf{E}^{int} = \mathbf{E}_0 \exp(ik\hat{e}^{int} \cdot \vec{r}) \tag{2.1}$$

where $\mathbf{E}_0$ is the amplitude of incident field. The convention $\exp(-i\omega t)$ (ω, angular frequency) is employed and always surpressed in the formulation. In the far-field region, the scattered electromagnetic field is a transverse spherical wave:

$$\mathbf{E}^{sca}|_{kr\to\infty} = \frac{\exp(ikr)}{-ikr}\mathbf{E}_1^{sca} \tag{2.2}$$

where r is the radial coordinate, k is the wavenumber of surrounding medium and $\mathbf{E}_1^{sca}$ is the amplitude of scattered electric field.

The amplitude of incident and scattering electric fields can be decomposed into parallel and perpendicular components relative to the scattering plane (Figure 2.1). The relationships between the unit vectors are defined as:

$$\hat{e}_\perp \times \hat{e}_\parallel^{sca} = \hat{e}^{sca}, \quad \hat{e}_\perp \times \hat{e}_\parallel^{inc} = \hat{e}^{inc} \tag{2.3}$$

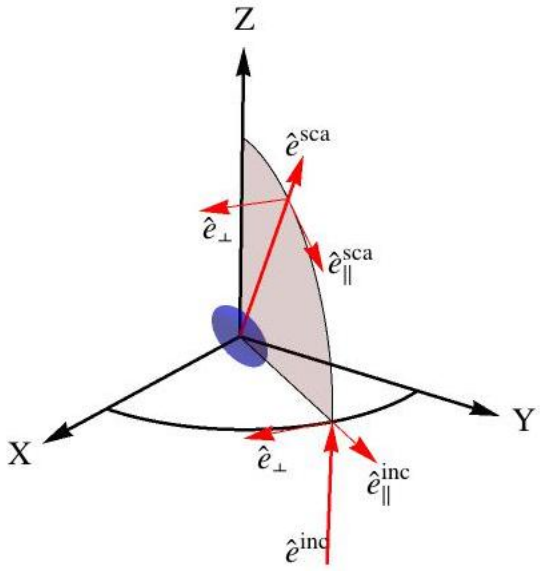

Figure 2.1: Decomposition of the amplitudes of incident and scattered electric fields associated with the scattering plane, which contains the incident and scattered direction. The incident direction is along the z-axis of the laboratory frame of reference.

There must be a linear relationship between incident and scattered electromagnetic fields due to the linearity of Maxwell's equations. Consequently, the amplitude scattering matrix **S** can be represented as [22, 23, 2]:

$$\begin{pmatrix} E_{\parallel}^{sca} \\ E_{\perp}^{sca} \end{pmatrix} = \frac{\exp(ik(r-z))}{-ikr} \begin{pmatrix} S_{11} & S_{12} \\ S_{21} & S_{22} \end{pmatrix} \begin{pmatrix} E_{\parallel}^{int} \\ E_{\perp}^{int} \end{pmatrix} \tag{2.4}$$

where the incident direction is along the z-axis of the laboratory frame of reference. All of the scattering information is contained in the matrix **S**. The four complex elements consists of eight independent constants. There are seven independent constants since only the relative phase is effective in scattering considerations. Amplitude scattering matrix is the relationship between electric fields. In measurements,

the quantity devices measure is energy or flux related.

The monochromatic Stokes vectors $(I\ Q\ U\ V)^T$, which represent energy flux, are defined as [24]:

$$I = E_{\parallel}E_{\parallel}^{*} + E_{\perp}E_{\perp}^{*} \tag{2.5}$$

$$Q = E_{\parallel}E_{\parallel}^{*} - E_{\perp}E_{\perp}^{*} \tag{2.6}$$

$$U = E_{\parallel}E_{\perp}^{*} + E_{\perp}E_{\parallel}^{*} \tag{2.7}$$

$$V = i(E_{\parallel}E_{\perp}^{*} - E_{\perp}E_{\parallel}^{*}) \tag{2.8}$$

The phase matrix (or Mueller matrix) is the relationship between incident and scattered Stokers vectors:

$$\begin{pmatrix} I_s \\ Q_s \\ U_s \\ V_s \end{pmatrix} = \frac{1}{k^2 r^2} \begin{pmatrix} P_{11} & P_{12} & P_{13} & P_{14} \\ P_{21} & P_{22} & P_{23} & P_{24} \\ P_{31} & P_{32} & P_{33} & P_{34} \\ P_{41} & P_{42} & P_{43} & P_{44} \end{pmatrix} \begin{pmatrix} I_i \\ Q_i \\ U_i \\ V_i \end{pmatrix} \tag{2.9}$$

Of 16 elements, only 7 are independent since the phase matrix elements can be

represented by the elements of the amplitude scattering matrix, which are:

$$P_{11} = \frac{1}{2}(|S_{11}|^2 + |S_{12}|^2 + |S_{21}|^2 + |S_{22}|^2) \tag{2.10}$$

$$P_{12} = \frac{1}{2}(|S_{11}|^2 - |S_{12}|^2 + |S_{21}|^2 - |S_{22}|^2) \tag{2.11}$$

$$P_{13} = Re(S_{11}S_{12}^* + S_{21}S_{22}^*) \tag{2.12}$$

$$P_{14} = Im(S_{11}S_{12}^* + S_{21}S_{22}^*) \tag{2.13}$$

$$P_{21} = \frac{1}{2}(|S_{11}|^2 + |S_{12}|^2 - |S_{21}|^2 - |S_{22}|^2) \tag{2.14}$$

$$P_{22} = \frac{1}{2}(|S_{11}|^2 - |S_{12}|^2 - |S_{21}|^2 + |S_{22}|^2) \tag{2.15}$$

$$P_{23} = Re(S_{11}S_{12}^* - S_{21}S_{22}^*) \tag{2.16}$$

$$P_{24} = Im(S_{11}S_{12}^* - S_{21}S_{22}^*) \tag{2.17}$$

$$P_{31} = Re(S_{11}S_{21}^* + S_{12}S_{22}^*) \tag{2.18}$$

$$P_{32} = Re(S_{11}S_{21}^* - S_{12}S_{22}^*) \tag{2.19}$$

$$P_{33} = Re(S_{11}S_{22}^* + S_{12}S_{21}^*) \tag{2.20}$$

$$P_{34} = Im(S_{11}S_{22}^* - S_{12}S_{21}^*) \tag{2.21}$$

$$P_{41} = Im(S_{11}^*S_{21} + S_{12}^*S_{22}) \tag{2.22}$$

$$P_{42} = Im(S_{11}^*S_{21} - S_{12}^*S_{22}) \tag{2.23}$$

$$P_{43} = Im(S_{11}^*S_{22} - S_{12}S_{21}^*) \tag{2.24}$$

$$P_{44} = Re(S_{11}^*S_{22} - S_{12}S_{21}^*) \tag{2.25}$$

There must exist nine independent relationships which connect the elements [25]. The Mueller matrix includes all the scattering information as the amplitude scattering matrix does.

The integrated scattering quantities, scattering, absorption, and extinction cross sections, associated with a range of sizes also play an important role in scattering study. They are defined as the total scattered, absorbed, and removed monochromatic powers from the original beam divided by the monochromatic energy flux of the incident wave [22, 2]. The scattering and extinction cross section can be formulated using the amplitude of incident and scattered fields [2]:

$$C_{sca} = \frac{1}{k^2|\mathbf{E}_0^{inc}|^2}\int_{4\pi} d\Omega|\mathbf{E}_1^{sca}|^2 \tag{2.26}$$

$$C_{ext} = \frac{4\pi}{k^2|\mathbf{E}_0^{inc}|^2} Re[\mathbf{E}_1^{sca}(\hat{e}^{int})\cdot\mathbf{E}_0^{inc*}] \tag{2.27}$$

where Eqs.(2.1) and (2.2) have been used. Eq.(2.27) is also called the optical theorem, in which the extinction cross section is only related to the exact forward scattering even though the extinction is the combined effect of scattering and absorption. Due to energy conservation, the absorption cross section is the difference between the extinction and scattering cross section.

2.2 T-matrix method and symmetries

Many methods have been developed to obtain the amplitude scattering matrix or Mueller matrix of a single scatterer. For homogeneous spherical particles, an analytic solution, so-called Lorenz-Mie theory [22, 23], has been obtained. The whole range of sizes for homogeneous spherical or multiple-shell spherical particles can be calculated due to the improvement by Wiscombe [26]. For non-spherical particles, an theoretical solution has been obtained for homogeneous spheroids in terms of spheroidal coordinates by Asano et. al [27, 28]. Several numerically accurate methods have been developed to obtain light scattering properties by small particles, such as the finite-difference time domain method [29, 30], the discrete dipole approximation

method [31] and the pseudo spectral time-domain method [32].

Of the calculation methods for the scattering of non-spherical particles, a semi-analytical method, called T-matrix, is one of the most efficients methods, especially, for scatterers with axial or N-fold rotational symmetries. A transition matrix (T-matrix) associated with incident and scattered fields, which is independent of incident direction, can be achieved. Immediately, the random orientation can be analytically reached [33, 34] and the scattering in arbitrary fixed orientations can be obtained [35]. This is a great advantage obtaining the scattering results with random orientations compared to the numerically accurate methods, which need the incident direction for the calculation of arbitrary fixed orientation. Extended boundary condition method (EBCM), which was proposed by Waterman [4, 5] and greatly generalized by Mishchenko [2], and Invariant imbedding T-matrix method (II-TM), which was proposed by Johnson [6] and numerically implemented by Bi et.al and applied to many shapes of scatterers [7, 36, 37, 34], are currently two of the most effective realizations.

2.2.1 T-matrix method

Before introducing the T-matrix method, the matrices associated with solid angles are defined in spherical coordinates for convenience [6]:

$$\mathbf{A}_{mn}(\theta,\varphi) = (-1)^m \gamma_n \exp(im\varphi) \begin{pmatrix} 0 \\ i\pi_{mn}(\theta) \\ -\tau_{mn}(\theta) \end{pmatrix} \tag{2.28}$$

$$\mathbf{B}_{mn}(\theta,\varphi) = (-1)^m \gamma_n \exp(im\varphi) \begin{pmatrix} 0 \\ \tau_{mn}(\theta) \\ i\pi_{mn}(\theta) \end{pmatrix} \tag{2.29}$$

$$\mathbf{C}_{mn}(\theta,\varphi) = (-1)^m \gamma_n \exp(im\varphi) \begin{pmatrix} \sqrt{n(n+1)} d^n_{0m}(\theta) \\ 0 \\ 0 \end{pmatrix} \tag{2.30}$$

$$\mathbf{Y}_{mn}(\theta,\varphi) = [\mathbf{A}_{mn}(\theta,\varphi), \mathbf{B}_{mn}(\theta,\varphi), \mathbf{C}_{mn}(\theta,\varphi)] \tag{2.31}$$

where θ and φ are polar or zenith and azimuthal angles, $\gamma_n = \sqrt{\frac{2n+1}{4\pi n(n+1)}}$, and $\pi_{mn}(\theta)$, $\tau_{mn}(\theta)$, and, $d^n_{om}(\theta)$ are formulated as follows [2]:

$$d^n_{0m}(\theta) = (-1)^m \sqrt{\frac{(n-m)!}{(n+m)!}} P^m_n(\theta) \tag{2.32}$$

$$\pi_{mn}(\theta) = \frac{m}{\sin\theta} d^n_{0m}(\theta) \tag{2.33}$$

$$\tau_{mn}(\theta) = \frac{d}{d\theta} d^n_{0m}(\theta) \tag{2.34}$$

where $P^m_n(\cos\theta)$ is the associated Legendre function. The matrix associated with radial coordinates are defined as [6]:

$$\mathbf{Z}_n(kr) = \begin{pmatrix} z_n(kr) & 0 \\ 0 & \frac{1}{kr}\frac{d}{d(kr)}(krz_n(kr)) \\ 0 & \frac{\sqrt{n(n+1)}}{kr} z_n(kr) \end{pmatrix} \tag{2.35}$$

where $\mathbf{Z}_n(kr)$ represents the two kinds of Bessel functions ($\mathbf{J}$ for Bessel function and $\mathbf{H}$ for the Hankel function of the first kind).

The vector spherical wave functions are as follows [2]:

$$(Rg\mathbf{M}_{mn}(r,\Omega), Rg\mathbf{N}_{mn}(r,\Omega)) = \mathbf{Y}_{mn}(\Omega)\mathbf{J}_n(r) \tag{2.36}$$

$$(\mathbf{M}_{mn}(r,\Omega), \mathbf{N}_{mn}(r,\Omega)) = \mathbf{Y}_{mn}(\Omega)\mathbf{H}_n(r) \tag{2.37}$$

where $Rg\mathbf{M}$ and $Rg\mathbf{N}$ represent the regular ones, which are finite at the origin

($\vec{r} = \vec{0}$), and $\mathbf{M}$ and $\mathbf{N}$ are the outgoing ones, which are proportional to $1/kr$ for the transverse components and to the high order of $1/kr$ for the longitudinal components in the far field region.

Consequently, incident and scattered fields can be expanded by the vector spherical wave functions as follows:

$$\mathbf{E}^{inc} = \sum_{n=1}^{\infty} \sum_{m=-n}^{n} [a_{mn} Rg\mathbf{M}_{mn}(k\vec{r}) + b_{mn} Rg\mathbf{N}_{mn}(k\vec{r})] \tag{2.38}$$

$$\mathbf{E}^{sca} = \sum_{n=1}^{\infty} \sum_{m=-n}^{n} [p_{mn}\mathbf{M}_{mn}(k\vec{r}) + q_{mn}\mathbf{N}_{mn}(k\vec{r})], r > r_{>} \tag{2.39}$$

where $r_{>}$ is the radius of the circumscribed sphere of a single scatterer and, a_{mn}, b_{mn}, and, p_{mn}, q_{mn} are expansion coefficients for incident and scattered fields, respectively. In terms of Eq.(2.1), the expansion coefficients of the incident field are formulated as follows [38, 1, 2]:

$$a_{mn} = 4\pi i^n \mathbf{E}_0 \cdot \mathbf{A}^*_{mn}(\theta^{inc}, \varphi^{inc}) \tag{2.40}$$

$$b_{mn} = 4\pi i^{n-1} \mathbf{E}_0 \cdot \mathbf{B}^*_{mn}(\theta^{inc}, \varphi^{inc}) \tag{2.41}$$

where Eqs.(2.28) and (2.29) have been used and $(\theta^{inc}, \varphi^{inc})$ are the incident zenith and azimuthal angles relative to the laboratory frame of reference.

Due to the linearity of maxwell's equations, there must exist a linear relationship between the expansion coefficients of incident and scattered fields, called T-matrix $\mathbf{T}$:

$$\begin{pmatrix} p_{mn} \\ q_{mn} \end{pmatrix} = \sum_{n'=1}^{\infty} \sum_{m'=-n'}^{n'} \begin{pmatrix} T^{11}_{mnm'n'} & T^{12}_{mnm'n'} \\ T^{21}_{mnm'n'} & T^{22}_{mnm'n'} \end{pmatrix} \begin{pmatrix} a_{m'n'} \\ b_{m'n'} \end{pmatrix} \tag{2.42}$$

Generally, T-matrix associated with different azimuthal terms (denoted by m and

m') are fully coupled for an arbitrary scatterer; however, for scatterers with N-fold rotational symmetry, the T-matrix can be partially decoupled. For scatterers with axial rotational symmetry, it is fully decoupled in terms of m.

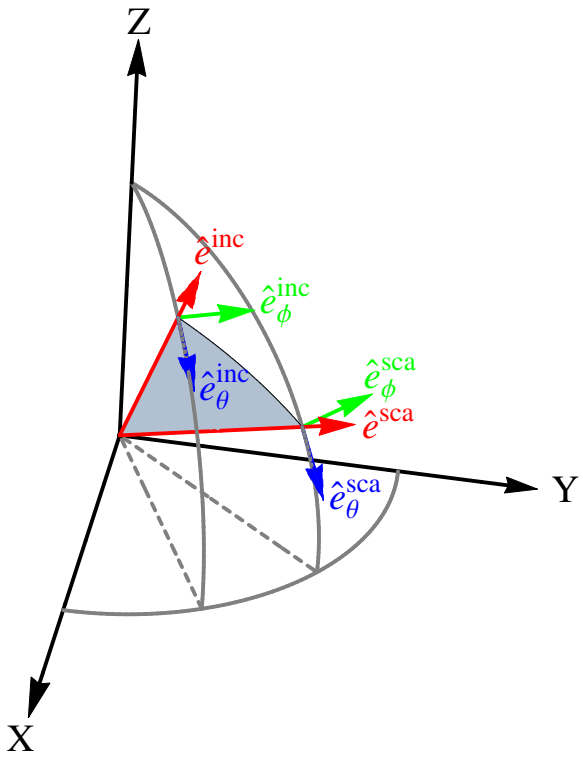

Figure 2.2: Decomposition of the amplitudes of incident and scattered electric fields associated with their meridional planes, which contain the z-axis of the laboratory frame of reference and the incident or scattered directions.

Another kind of amplitude scattering matrix is represented in terms of the merid-

ional planes (Figure 2.2) of the incident and scattered fields [2]:

$$\begin{pmatrix} E_\theta^{sca} \\ E_\varphi^{sca} \end{pmatrix} = \frac{\exp(ikr)}{-ikr} \begin{pmatrix} S_{11}^M & S_{12}^M \\ S_{21}^M & S_{22}^M \end{pmatrix} \begin{pmatrix} E_\theta^{int} \\ E_\varphi^{int} \end{pmatrix} \tag{2.43}$$

In terms of Eqs.(2.38), (2.39), (2.40), (2.41), (2.42) and (2.43), the amplitude scattering matrix can be formulated as follows [2]:

$$\begin{aligned} S_{11}^M(\hat{e}^{sca}, \hat{e}^{inc}) = \sum_{mnm'n'} \alpha_{mnm'n'} [T_{mnm'n'}^{11} \pi_{mn}(\theta^{sca}) \pi_{m'n'}(\theta^{inc}) \\ + T_{mnm'n'}^{12} \pi_{mn}(\theta^{sca}) \tau_{m'n'}(\theta^{inc}) + T_{mnm'n'}^{21} \tau_{mn}(\theta^{sca}) \pi_{m'n'}(\theta^{inc}) \\ + T_{mnm'n'}^{22} \tau_{mn}(\theta^{sca}) \tau_{m'n'}(\theta^{inc})] \exp[i(m\varphi^{sca} - m'\varphi^{inc})] \end{aligned} \tag{2.44}$$

$$\begin{aligned} S_{12}^M(\hat{e}^{sca}, \hat{e}^{inc}) = -i \sum_{mnm'n'} \alpha_{mnm'n'} [T_{mnm'n'}^{11} \pi_{mn}(\theta^{sca}) \tau_{m'n'}(\theta^{inc}) \\ + T_{mnm'n'}^{12} \pi_{mn}(\theta^{sca}) \pi_{m'n'}(\theta^{inc}) + T_{mnm'n'}^{21} \tau_{mn}(\theta^{sca}) \tau_{m'n'}(\theta^{inc}) \\ + T_{mnm'n'}^{22} \tau_{mn}(\theta^{sca}) \pi_{m'n'}(\theta^{inc})] \exp[i(m\varphi^{sca} - m'\varphi^{inc})] \end{aligned} \tag{2.45}$$

$$\begin{aligned} S_{21}^M(\hat{e}^{sca}, \hat{e}^{inc}) = i \sum_{mnm'n'} \alpha_{mnm'n'} [T_{mnm'n'}^{11} \tau_{mn}(\theta^{sca}) \pi_{m'n'}(\theta^{inc}) \\ + T_{mnm'n'}^{12} \tau_{mn}(\theta^{sca}) \tau_{m'n'}(\theta^{inc}) + T_{mnm'n'}^{21} \pi_{mn}(\theta^{sca}) \pi_{m'n'}(\theta^{inc}) \\ + T_{mnm'n'}^{22} \pi_{mn}(\theta^{sca}) \tau_{m'n'}(\theta^{inc})] \exp[i(m\varphi^{sca} - m'\varphi^{inc})] \end{aligned} \tag{2.46}$$

$$\begin{aligned} S_{22}^M(\hat{e}^{sca}, \hat{e}^{inc}) = \sum_{mnm'n'} \alpha_{mnm'n'} [T_{mnm'n'}^{11} \tau_{mn}(\theta^{sca}) \tau_{m'n'}(\theta^{inc}) \\ + T_{mnm'n'}^{12} \tau_{mn}(\theta^{sca}) \pi_{m'n'}(\theta^{inc}) + T_{mnm'n'}^{21} \pi_{mn}(\theta^{sca}) \tau_{m'n'}(\theta^{inc}) \\ + T_{mnm'n'}^{22} \pi_{mn}(\theta^{sca}) \pi_{m'n'}(\theta^{inc})] \exp[i(m\varphi^{sca} - m'\varphi^{inc})] \end{aligned} \tag{2.47}$$

where $\sum_{mnm'n'}$ represents $\sum_{n=1}^{\infty} \sum_{m=-n}^{n} \sum_{n'=1}^{\infty} \sum_{m'=-n'}^{n'}$, $(\theta^{sca}, \varphi^{sca})$ are the scattered zenith and

azimuthal angles relative to the laboratory frame of reference and

$$\alpha_{mnm'n'} = i^{n'-n}(-1)^{m+m'+1}\sqrt{\frac{(2n+1)(2n'+1)}{n(n+1)n'(n'+1)}} \tag{2.48}$$

The amplitude scattering matrix relative to the scattering plane in Eq.(2.4) can be immediately obtained using the one relative to the meridional planes, and then the Mueller matrix.

The scattering and extinction cross sections can be represented in terms of the expansion coefficients of incident and scattered fields [2]:

$$C_{sca} = \frac{1}{k^2|\mathbf{E}_0^{inc}|^2}\sum_{n=1}^{\infty}\sum_{m=-n}^{n}[|p_{mn}|^2 + |q_{mn}|^2] \tag{2.49}$$

$$C_{ext} = -\frac{1}{k^2|\mathbf{E}_0^{inc}|^2}\sum_{n=1}^{\infty}\sum_{m=-n}^{n}Re[a_{mn}p_{mn}^* + b_{mn}q_{mn}^*] \tag{2.50}$$

2.2.2 Symmetry in T-matrix

No matter which T-matrix realization, EBCM or II-TM, is employed, matrix storage and inversions are necessary in the process of calculation. For scatterers with specific symmetries, the T-matrix can be partially or fully decoupled [3, 2]. After considering the symmetries, the calculation efficiency for T-matrix can be dramatically increased.

Generally, the calculation of T-matrix is in the particle frame of reference, which can take all particle symmetries into considerations. The T-matrix in the laboratory frame of reference can be obtained in terms of the rotation of the T-matrix in the particle frame of reference [39, 2, 3]:

$$T_{mnm'n'}^{lj}(L;\alpha,\beta,\gamma) = \sum_{m_1=-n}^{n}\sum_{m_2=-n'}^{n'}D_{mm_1}^{n}(\alpha,\beta,\gamma)T_{mnm'n'}^{lj}(P)D_{mm_1}^{n}(-\gamma,-\beta,-\alpha) \tag{2.51}$$

where $D^n_{mm_1}(\alpha,\beta,\gamma) = \exp(-im\alpha)d^n_{mm_1}(\beta)\exp(-im_1\gamma)$. $D^n_{mm_1}$ and $d^n_{mm_1}$ are the Wigner-D and Wigner-d functions [2]. α,β,γ are the Euler angles, which rotate the laboratory frame of reference into the particle frame of reference and use 'zyz' convention, which is first to rotate α angle relative to the z-axis of laboratory frame of reference, β angle relative to the new y-axis, and at last γ angle relative to the newest z-axis.

The rotation operation relative to the z-axis of particle frame of reference can be proceeded as $\alpha \neq 0$ and $\beta = \gamma = 0$:

$$T^{lj}_{mnm'n'} \rightarrow \exp[-i(m-m')\alpha]T^{lj}_{mnm'n'} \tag{2.52}$$

If a scatterer has a N-fold rotational symmetry along the z-axis(denoted as C_N), the T-matrix remains the same with the C_N operation ($\alpha = 2\pi/N$ according to Eq.(2.52)). The azimuthal terms must have the following relationship:

$$m - m' = N * k, k = 0, \pm 1, \pm 2, ... \tag{2.53}$$

The T-matrix is partially decoupled by the C_N symmetry. For instance, a hexagonal prism has a C_6 symmetry, which means $m - m' = 6k$ and the original T-matrix is decomposed into 6 sub-matrices. For scatterers with axial rotational symmetry, such as a right cylinder and a spheroid, or with a C_∞ symmetry, the T-matrix is fully decoupled according to the term m, that is, $T^{lj}_{mnm'n'} = T^{lj}_{mnmn'}$.

If a scatterer has a C_2 symmetry perpendicular to the z-axis of particle frame of reference, the T-matrix has the following relation [3]:

$$T^{lj}_{-mn-m'-n'} = (-1)^{(n+n')}(-1)^{(m+m')}T^{lj}_{mnm'n'} \tag{2.54}$$

For a horizontal reflection or mirror operation relative to the xoy plane of particle frame of reference (denoted as σ_h), T-matrix has the transition as follows [3]:

$$T^{lj}_{mnm'n'} \xrightarrow{\sigma_h} (-1)^{(m+m')}(-1)^{(n+n')}(-1)^{(l+j)}T^{lj}_{mnm'n'} \tag{2.55}$$

If a scatterer has the σ_h symmetry, for example a spheroid or a cylinder, half of the T-matrix elements has to be 0:

$$T^{lj}_{mnm'n'} = 0, \text{ if } (-1)^{(l+j)+(m+m\prime)+(n+n\prime)} = -1 \tag{2.56}$$

For two vertical refelction or mirror operations relative to xoz plane (denoted as σ_{xz}) and to yoz plane (denoted as σ_{yz}), T-matrix has the following transitions [3]:

$$T^{lj}_{-mn-m'-n'} = \begin{cases} \xrightarrow{\sigma_{xz}} & (-1)^{(m+m')}(-1)^{(l+j)}T^{lj}_{mnm'n'} \\ \xrightarrow{\sigma_{yz}} & (-1)^{(l+j)}T^{lj}_{mnm'n'} \end{cases} \tag{2.57}$$

If a scatterer has the σ_{xz} or the σ_{yz} symmetry, only parts of T-matrix need to be calculated if the T-matrix is decoupled associated with different m. For instance, the T-matrix of a spheroid is fully decoupled according to different azimuthal terms of m. Only the T-matrix with $m = 0, 1, 2, 3, ...$ needs to be calculated since the terms with $m = -1, -2, -3, ...$ can be obtained in terms of Eq.(2.57).

Only parts of symmetries associated with T-matrix are displayed in this subsection. The more detailed derivations and symmetries associated with T-matrix can be found in Schulz et. al [3] and Mishchenko et. al [2].

2.3 Extended boundary condition method (EBCM)

In terms of the vector Green's theorem, incident and scattered fields can be formulated as two surface integrals [38, 1, 2]:

$$\mathbf{E}^{sca}(\vec{r}') = \int_s ds\{i\omega\mu_0[\hat{n}\times\mathbf{H}_+(\vec{r})]\cdot\overleftrightarrow{\mathbf{G}}(\vec{r},\vec{r}') + [\hat{n}\times\mathbf{E}_+(\vec{r})]\cdot[\nabla\times\overleftrightarrow{\mathbf{G}}(\vec{r},\vec{r}')]\} \quad (2.58)$$

$$\mathbf{E}^{inc}(\vec{r}') = -\int_s ds\{i\omega\mu_0[\hat{n}\times\mathbf{H}_+(\vec{r})]\cdot\overleftrightarrow{\mathbf{G}}(\vec{r},\vec{r}') + [\hat{n}\times\mathbf{E}_+(\vec{r})]\cdot[\nabla\times\overleftrightarrow{\mathbf{G}}(\vec{r},\vec{r}')]\} \quad (2.59)$$

where $\vec{r}'$ is in the exterior region of a scatterer for $\mathbf{E}^{sca}(\vec{r}')$ and in the interior region for $\mathbf{E}^{inc}(\vec{r}')$, the permeability μ has been assumed to be the μ_0 in vacuum, the integration surface s encloses the volume of the scatterer and the subscript '+' represents the exterior side of the surface s, and, $\overleftrightarrow{\mathbf{G}}$ is the dyadic green function, which can be expanded in terms of vector spherical wave functions [2, 6]:

$$\overleftrightarrow{\mathbf{G}}(\vec{r},\vec{r}') = \sum_{mn}\mathbf{Y}_{mn}(\Omega)\mathbf{g}_n(r,r')\mathbf{Y}^{\dagger}_{mn}(\Omega') \quad (2.60)$$

$$\mathbf{g}_n(r,r') = \begin{cases} ik\mathbf{H}_n(r)\mathbf{J}_n^T(r'), & r > r' \\ ik[\mathbf{H}_n(r)\mathbf{J}_n^T(r') + \mathbf{J}_n(r)\mathbf{H}_n^T(r')]/2, & r = r' \\ ik\mathbf{J}_n(r)\mathbf{H}_n^T(r'), & r < r' \end{cases} \quad (2.61)$$

where Eq.(2.31) has been used, † represents the operations of complex conjugation and transpose and T the transpose operation.

In terms of Eqs.(2.38), (2.39), (2.60) and (2.61), the expansion coefficients of

incident and scattered fields can be formulated as surface integrals [2]:

$$\begin{pmatrix} a_{mn} \\ b_{mn} \end{pmatrix} = (-1)^m k \int_s ds\{\omega\mu_0[\hat{n} \times \mathbf{H}_+(\vec{r})] \begin{pmatrix} \mathbf{M}_{-mn}(kr,\theta,\varphi) \\ \mathbf{N}_{-mn}(kr,\theta,\varphi) \end{pmatrix} - ik[\hat{n} \times \mathbf{E}_+(\vec{r})] \begin{pmatrix} \mathbf{N}_{-mn}(kr,\theta,\varphi) \\ \mathbf{M}_{-mn}(kr,\theta,\varphi) \end{pmatrix}\} \tag{2.62}$$

$$\begin{pmatrix} p_{mn} \\ q_{mn} \end{pmatrix} = (-1)^m k \int_s ds\{\omega\mu_0[\hat{n} \times \mathbf{H}_+(\vec{r})] \begin{pmatrix} Rg\mathbf{M}_{-mn}(kr,\theta,\varphi) \\ Rg\mathbf{N}_{-mn}(kr,\theta,\varphi) \end{pmatrix} - ik[\hat{n} \times \mathbf{E}_+(\vec{r})] \begin{pmatrix} Rg\mathbf{N}_{-mn}(kr,\theta,\varphi) \\ Rg\mathbf{M}_{-mn}(kr,\theta,\varphi) \end{pmatrix}\} \tag{2.63}$$

The interior electromagnetic field of the scatterer, supposed, can be expanded in terms of regular vector spherical wave functions [2]:

$$\mathbf{E}^{int}(\vec{r}) = \sum_{mn}[c_{mn}Rg\mathbf{M}_{mn}(k_1\vec{r}) + d_{mn}Rg\mathbf{N}_{mn}(k_1\vec{r})] \tag{2.64}$$

$$\mathbf{H}^{int}(\vec{r}) = \frac{k_1}{i\omega\mu_0}\sum_{mn}[d_{mn}Rg\mathbf{M}_{mn}(k_1\vec{r}) + c_{mn}Rg\mathbf{N}_{mn}(k_1\vec{r})] \tag{2.65}$$

where k_1 is the wavenumber in the scattering medium, and c_{mn} and d_{mn} are the expansion coefficients of interior electromagnetic field.

The Maxwell's boundary conditions in the surface s are employed:

$$\begin{aligned} \nabla \times \mathbf{E}_+ &= \nabla \times \mathbf{E}_- \\ \nabla \times \mathbf{H}_+ &= \nabla \times \mathbf{H}_- \end{aligned} \tag{2.66}$$

where the subscript '-' represents the interior side of surface s.

In terms of Eqs.(2.62), (2.63), (2.64), (2.65) and (2.66), two relationships as-

sociated with the expansion coefficients of between incident and interior fields and between scattering and interior fields can be represented as matrix forms [2]:

$$\begin{pmatrix} \mathbf{a} \\ \mathbf{b} \end{pmatrix} = \begin{pmatrix} \mathbf{Q}_{11} & \mathbf{Q}_{12} \\ \mathbf{Q}_{21} & \mathbf{Q}_{22} \end{pmatrix} \begin{pmatrix} \mathbf{c} \\ \mathbf{d} \end{pmatrix} \tag{2.67}$$

$$\begin{pmatrix} \mathbf{p} \\ \mathbf{q} \end{pmatrix} = - \begin{pmatrix} Rg\mathbf{Q}_{11} & Rg\mathbf{Q}_{12} \\ Rg\mathbf{Q}_{21} & Rg\mathbf{Q}_{22} \end{pmatrix} \begin{pmatrix} \mathbf{c} \\ \mathbf{d} \end{pmatrix} \tag{2.68}$$

where

$$(Rg)Q^{11}_{mnm'n'} = -ikk_1(Rg)J^{21}_{mnm'n'} - ik^2(Rg)J^{12}_{mnm'n'} \tag{2.69}$$

$$(Rg)Q^{12}_{mnm'n'} = -ikk_1(Rg)J^{11}_{mnm'n'} - ik^2(Rg)J^{22}_{mnm'n'} \tag{2.70}$$

$$(Rg)Q^{21}_{mnm'n'} = -ikk_1(Rg)J^{22}_{mnm'n'} - ik^2(Rg)J^{11}_{mnm'n'} \tag{2.71}$$

$$(Rg)Q^{22}_{mnm'n'} = -ikk_1(Rg)J^{12}_{mnm'n'} - ik^2(Rg)J^{21}_{mnm'n'} \tag{2.72}$$

and

$$(Rg)J^{11}_{mnm'n'} = (-1)^m \int_s ds\hat{n} \cdot [Rg\mathbf{M}_{m'n'}(k_1\vec{r}) \times (Rg)\mathbf{M}_{-mn}(k\vec{r})] \tag{2.73}$$

$$(Rg)J^{12}_{mnm'n'} = (-1)^m \int_s ds\hat{n} \cdot [Rg\mathbf{M}_{m'n'}(k_1\vec{r}) \times (Rg)\mathbf{N}_{-mn}(k\vec{r})] \tag{2.74}$$

$$(Rg)J^{21}_{mnm'n'} = (-1)^m \int_s ds\hat{n} \cdot [Rg\mathbf{N}_{m'n'}(k_1\vec{r}) \times (Rg)\mathbf{M}_{-mn}(k\vec{r})] \tag{2.75}$$

$$(Rg)J^{22}_{mnm'n'} = (-1)^m \int_s ds\hat{n} \cdot [Rg\mathbf{N}_{m'n'}(k_1\vec{r}) \times (Rg)\mathbf{N}_{-mn}(k\vec{r})] \tag{2.76}$$

The T-matrix can be formally expressed as follows:

$$\mathbf{T} = -(Rg\mathbf{Q})\mathbf{Q}^{-1} \tag{2.77}$$

where **a** and **b**, **c** and **d**, and **p** and **q**, are the corresponding matrix expressions of the expansion coefficients of incident, interior, and scattering fields.

The gist of the EBCM is constructing the relationships between incident and interior fields, and between scattering and interior fields in terms of boundary conditions. Then the T-matrix can be obtained in term of an matrix inversion.

2.4 Invariant imbedding T-matrix method

The invariant imbedding T-matrix method is based on the volume integral equation of electromagnetic field [40]:

$$\mathbf{E}(\vec{r}) = \mathbf{E}^{inc}(\vec{r}) + \int_V d^3r' \overleftrightarrow{\mathbf{G}}_1 (\vec{r},\vec{r}) u(\vec{r}') \mathbf{E}(\vec{r}') \tag{2.78}$$

where $u(\vec{r}') = k^2(\epsilon(\vec{r}) - 1)$ and ϵ is the permittivity of a scatterer, the dyadic green function in the volume integral contains a singular term [1]:

$$\overleftrightarrow{\mathbf{G}}_1 (\vec{r},\vec{r}') = \overleftrightarrow{\mathbf{G}} (\vec{r},\vec{r}') - \frac{\delta(\vec{r}-\vec{r}')}{k^2} \hat{r}\hat{r} \tag{2.79}$$

where Eqs.(2.60) and (2.61) have been used. Taking the singularity into consideration, Eq.(2.78) can be rearranged as [6]:

$$\bar{\mathbf{E}}(\vec{r}) = \mathbf{E}^{inc}(\vec{r}) + \int_V d^3r' \overleftrightarrow{\mathbf{G}} (\vec{r},\vec{r}) u(\vec{r}') \mathbf{Z}(\vec{r}') \bar{\mathbf{E}}(\vec{r}') \tag{2.80}$$

where

$$\mathbf{Z}(\vec{r}) = \begin{pmatrix} 1/\epsilon(\vec{r}) & 0 & 0 \\ 0 & 1 & 0 \\ 0 & 0 & 1 \end{pmatrix} \tag{2.81}$$

$$\mathbf{E}(\vec{r}) = \mathbf{Z}(\vec{r}) \bar{\mathbf{E}}(\vec{r}) \tag{2.82}$$

Outside the scatterer, the effective electric field $\bar{\mathbf{E}}$ is actually the same as $\mathbf{E}$. In convenience, we will substitute the signal $\mathbf{E}$ for $\bar{\mathbf{E}}$ in the following introduction.

The incident and scattered fields will have the expansions as Eqs.(2.38) and (2.39) do. Due to the linearity between scattered and incident electric fields, we can assign the incident wave as a single multipole component. The volume integral Eq.(2.80) can be presented as the single multipole component:

$$\mathbf{E}_{m'n'}(r,\Omega) = \mathbf{Y}_{m'n'}(\Omega)\mathbf{J}_{n'}(r) + \int_0^R dr' \sum_{mn} \mathbf{Y}_{mn}(\Omega)\mathbf{g}_n(r,r')\mathbf{F}_{mnm'n'}(r',\Omega') \quad (2.83)$$

where R is the radius of circumscribed sphere and the vector field $\mathbf{F}$ is defined as:

$$\mathbf{F}_{mnm'n'}(r) = r^2 \int d\Omega \mathbf{Y}^{\dagger}_{mn}(\Omega)u(r,\Omega)\mathbf{Z}(r,\Omega)\mathbf{E}_{m'n'}(r,\Omega) \quad (2.84)$$

The vector field $\mathbf{F}$ can also be formulated in terms of Eq.(2.83) as the form of a Fredholm equation [41]:

$$\mathbf{F}_{mnm'n'}(r) = \mathbf{U}_{mnm'n'}(r)\mathbf{J}_{n'}(r) + \int_0^R dr' \sum_{m_1n_1} \mathbf{U}_{mnm_1n_1}(r)\mathbf{g}_{n_1}(r,r')\mathbf{F}_{m_1n_1m'n'}(r') \quad (2.85)$$

where

$$\mathbf{U}_{mnm'n'}(r) = r^2 \int d\Omega \mathbf{Y}^{\dagger}_{mn}(\Omega)u(r,\Omega)\mathbf{Z}(r,\Omega)\mathbf{Y}_{m'n'}(\Omega) \quad (2.86)$$

For the far field region, $r \gg r'$. In terms of Eqs.(2.61), Eq.(2.83) can be formally represented as follows:

$$\mathbf{E}_{m'n'}(r,\Omega) = \mathbf{Y}_{m'n'}(\Omega)\mathbf{J}_{n'}(r) + \sum_{mn} \mathbf{Y}_{mn}(\Omega)\mathbf{H}_n(r)\mathbf{T}_{mnm'n'} \quad (2.87)$$

where

$$\mathbf{T}_{mnm'n'} = ik \int_0^R dr \mathbf{J}^T_n(r)\mathbf{F}_{mnm'n'}(r) \quad (2.88)$$

Using matrix expressions and numerical quadrature formulas, Eqs.(2.85) and (2.88) can be transformed into summations:

$$\mathbf{F}(r_i) = \mathbf{U}(r_i)\mathbf{J}(r_i) + \sum_{j=1}^{N} \omega_j \mathbf{U}(r_i)\mathbf{g}(r_i, r_j)\mathbf{F}(r_j) \tag{2.89}$$

$$\mathbf{T} = ik \sum_{j=1}^{N} \omega_j \mathbf{J}^T(r_j)\mathbf{F}(r_j) \tag{2.90}$$

where r_i and ω_i are quadrature points and wights, respectively. Eqs.(2.89) and

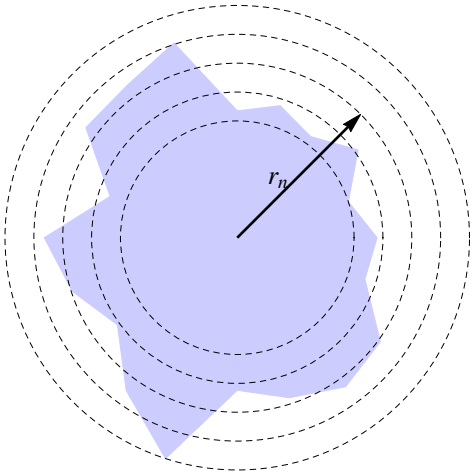

Figure 2.3: Systematic diagram for invariant imbedding process. The blue area represents the scatterer and the dashed lines represent the invariant imbedding process.

(2.90) are the key equations to execute the imbedding processes [6, 42]. When the imbedding process has reached the n-th layer, Eqs.(2.89) and (2.90) are set to be as

follows for $1 \leq n \leq N$:

$$\mathbf{F}(n|r_i) = \mathbf{U}(r_i)\mathbf{J}(r_i) + \sum_{j=1}^{n} \omega_j \mathbf{U}(r_i)\mathbf{g}(r_i, r_j)\mathbf{F}(n|r_j),\ i = 1, ..., n \tag{2.91}$$

$$\mathbf{T}(r_n) = ik \sum_{j=1}^{n} \omega_j \mathbf{J}^T(r_j)\mathbf{F}(n|r_j) \tag{2.92}$$

The transmission of the electric field in the n-th layer is set to be $\mathbf{L}_T$. Consequently, the recurrence relation of the field $\mathbf{F}$ should be:

$$\mathbf{F}(n|r_i) = \mathbf{F}(n-1|r_i)(\mathbf{I} + \mathbf{L}_T) \tag{2.93}$$

where $\mathbf{I}$ is a unit matrix.

For $i = n$, Eq.(2.91) can be transformed as follows:

$$\mathbf{F}(n|r_n) = \omega_n^{-1}\mathbf{Q}(r_n)[\mathbf{J}(r_n) + \mathbf{H}(r_n)\mathbf{L}_R] \tag{2.94}$$

where Eq.(2.61) has been used, and,

$$\mathbf{Q}(r_n) = \omega_n[\mathbf{I} - \omega_n \mathbf{U}(r_n)\mathbf{g}(r_n, r_n)]^{-1}\mathbf{U}(r_n) \tag{2.95}$$

$$\mathbf{L}_R = ik \sum_{j=1}^{n-1} \omega_j \mathbf{J}(r_j)\mathbf{F}(n|r_j) \tag{2.96}$$

where the physical meaning of $\mathbf{L}_R$ is the reflection coefficient of the electric field in the n-th layer.

For $1 \leq i \leq n-1$, Eq.(2.91) can be formulated as:

$$\mathbf{L}_T = \mathbf{Q}_{12} + \mathbf{Q}_{11}\mathbf{L}_R \tag{2.97}$$

where Eqs.(2.91), (2.93) and (2.94) have been used, and,

$$\mathbf{Q}_{11}(r_n) = ik\mathbf{H}^T(r_n)\mathbf{Q}(r_n)\mathbf{H}(r_n) \tag{2.98}$$

$$\mathbf{Q}_{12}(r_n) = ik\mathbf{H}^T(r_n)\mathbf{Q}(r_n)\mathbf{J}(r_n) \tag{2.99}$$

In terms of Eqs.(2.93) and (2.94), Eq.(2.96) and (2.92) can be formulated as follows:

$$\mathbf{T}(r_n) = \mathbf{Q}_{22} + (\mathbf{I} + \mathbf{Q}_{21})\mathbf{L}_R \tag{2.100}$$

$$\mathbf{L}_R = \mathbf{T}(r_{n-1})(\mathbf{I} + \mathbf{L}_T) \tag{2.101}$$

where

$$\mathbf{Q}_{21}(r_n) = ik\mathbf{J}^T(r_n)\mathbf{Q}(r_n)\mathbf{H}(r_n) \tag{2.102}$$

$$\mathbf{Q}_{22}(r_n) = ik\mathbf{J}^T(r_n)\mathbf{Q}(r_n)\mathbf{J}(r_n) \tag{2.103}$$

In terms of Eqs.(2.97), (2.100) and (2.101), the T-matrix with n shells can be obtained in terms of the one with $(n-1)$ shells and functions associated with the n-th shell:

$$\mathbf{T}(r_n) = \mathbf{Q}_{22}(r_n) + (\mathbf{I} + \mathbf{Q}_{21}(r_n))[\mathbf{I} - \mathbf{T}(r_{n-1})\mathbf{Q}_{11}(r_n)]^{-1}\mathbf{T}(r_{n-1})(\mathbf{I} + \mathbf{Q}_{12}(r_n)) \tag{2.104}$$

Only function $\mathbf{U}$ defined in Eq.(2.86) contains the information of the refractive index of a scatterer. The T-matrix of inhomogenous scatterers can also be obtained by the II-TM by applying the corresponding refractive index associated with different positions on function $\mathbf{U}$.

The vector spherical wave functions are series with infinite orders. In a numerical

calculation, the order has to be truncated only if convergent results can be obtained. The truncation order is empirically taken referring to the truncation of Lorenz-Mie theory [26].

2.5 Conlcusion

The EBCM is based on the surface integral equation while the II-TM on the volume integral equation of electromagnetic field. The calculation speed of EBCM is faster than the one of II-TM, because the EBCM only needs to do matrix inversion once whereas the II-TM needs many matrix inversions to progress the imbedding process; however, the II-TM is more stable than the EBCM since the inverse process of the II-TM is only related to the Bessel functions with the same radial coordinate while the EBCM to the Bessel functions with the radial coordinates in the surface region. Numerically, the condition number for the II-TM inverse is smaller than the one of the EBCM inverse.

3. SCATTERING BY FINITE SCATTERER WITH LARGE ASPECT RATIO USING MANY BODY ITERATIVE T-MATRIX METHOD (MBIT)*

3.1 Introduction

The single-scattering properties of small particles are the foundation blocks of both radiative transfer simulation and remote sensing implementation and have been studied for many years. The Lorenz-Mie theory [22, 23] offers an analytic solution for the scattering properties of a sphere. When non sphericity is involved, a non-physical model allowing an analytic solution is an infinite right circular cylinder [22, 23] , which is a valid approximation when the ratio of the height to the diameter of the cross section is much larger than unity. Using the separation of variables technique in the corresponding coordinates, the analytic solution for a spheroid can be obtained in terms of an analytic series [27, 28, 43]. In addition to the analytic approaches, other accurate numerical methods, such as the finite-difference time domain (FDTD) method [29, 30, 44], the discrete dipole approximation (DDA) method [31, 45, 46], and the pseudo-spectral time domain (PSTD) method [32, 47, 48], have been used extensively for scattering computations. For particles with size parameters less than 100, these methods are preferred to calculate the scattering properties. However, for size parameters larger than 100, the aforementioned methods become impractical, and the geometric optics method in terms of the ray tracing technique is a reasonable alternative [49, 50, 51, 52]. Note that this method is capable of giving quite accurate results for size parameters on the order of 30, but the physical rationale remains an enigma [50, 52].

*Reprinted with permission from "Many-body iterative T-matrix method for large aspect ratio particles" by B. Sun, P. Yang, and G. W. Kattawar. J. Quant. Spectrosc. Radiat. Transfer, **127**, 165-175. Copyright 2013 @Elsevier.

The T-matrix is another semi-analytic technique. The most efficient scheme to obtain the T-matrix is the extended boundary condition method (EBCM), initially proposed by Waterman [4, 5]. The T-matrix depends on the physical properties of a particle, such as the refractive index, size parameter, and particle shape, but not on the incident field. In principle, EBCM can be applied to particles with arbitrary shapes, even to composite objects [53, 54]. This method is extremely powerful when the scattering particle is rotationally symmetric, such as a spheroid, a circular cylinder, and a Chebyshev particle [33, 55, 56, 57, 58]; however, numerical stability deteriorates with increased aspect ratios. Some researchers used the discrete sources method in order to alleviate the numerical difficulty [59]. In this study, we employ the many-body iterative T-matrix (MBIT) method, initially introduced by Yan et al. [8, 60]. In the following parts, we will discuss the method and illustrate some simulations based on the approach.

3.2 The MBIT method

In the T-matrix method, the incident and scattered electric fields are expanded in terms of the vector spherical wave functions [2] in the form:

$$\mathbf{E}^{inc}(k\vec{r}) = \sum_{n=1}^{\infty}\sum_{m=-n}^{n}\left[a_{mn}\mathbf{RgM}_{mn}(k\vec{r}) + b_{mn}\mathbf{RgN}_{mn}(k\vec{r})\right] \tag{3.1}$$

$$\mathbf{E}^{sca}(k\vec{r}) = \sum_{n=1}^{\infty}\sum_{m=-n}^{n}\left[p_{mn}\mathbf{M}_{mn}(k\vec{r}) + q_{mn}\mathbf{N}_{mn}(k\vec{r})\right],\ r > r_{>} \tag{3.2}$$

where k and $r_{>}$ denote the wave number in a vacuum and the radius of the smallest circumscribed sphere of the scatterer; $\mathbf{RgM}_{mn}$, $\mathbf{RgN}_{mn}$, $\mathbf{M}_{mn}$ and $\mathbf{N}_{mn}$ are the vector spherical wave functions; and, a_{mn} and b_{mn}, and p_{mn} and q_{mn} are the corresponding incident and scattering expansion coefficients. The specific definitions of vector spherical wave functions and expansion coefficients of the incident plane wave

can be found in [2]. The scattered electric field in the region between the surface and the smallest circumscribed sphere of a scatterer cannot be expanded in terms of outgoing spherical wave functions, $\mathbf{M}_{mn}$ and $\mathbf{N}_{mn}$ [2]. Consequently, the restriction of many-body scattering calculations using the vector spherical wave functions is that the smallest circumscribed spheres of particles do not intersect.

The expansion coefficients of the incident and scattered fields can be connected by the transition matrix or T-matrix, which is normally obtained in terms of the EBCM [4, 5, 2]:

$$\begin{pmatrix} p_{mn} \\ q_{mn} \end{pmatrix} = \sum_{n'=1}^{\infty} \sum_{m'=-n'}^{n'} \begin{pmatrix} T^{11}_{mnm'n'} & T^{12}_{mnm'n'} \\ T^{11}_{mnm'n'} & T^{12}_{mnm'n'} \end{pmatrix} \begin{pmatrix} a_{m'n'} \\ b_{m'n'} \end{pmatrix} \tag{3.3}$$

In practical calculations, the infinite expansion series are truncated for the sake of numerical stability. The order of the expansion term at which the truncation is performed is closely related to the particle refractive index, size, and shape. The particle aspect ratio is one of the most significant factors influencing the T-matrix convergence. A major numerical procedure of the T-matrix method is matrix inversion. When the characteristic aspect ratio is much larger than unity, the matrix dimension becomes so large that the T-matrix computation diverges due to the loss of numerical precision in the matrix inversion procedure. The MBIT method can be employed to alleviate the divergence problem and to calculate prolate particles with relatively large aspect ratios. In this method, the prolate particle is artificially divided into N sub-particles in the direction of the rotational axis in order for each sub-particle to remain rotationally invariant, and there are 2N frames of reference: N frames for N sub-particles and N frames for the original particle. We assume that the 2N frames of reference have the same spatial orientations. For every sub-particle,

the surface consists of two parts: the primary part from the surface of the original particle and the second from the artificial boundary, which are denoted, respectively, in terms of superscripts p and b in the present formalism based on the notations used in [8]. Figure 3.1 shows the schematic divisions of a spheroid and a cylinder, where b and p, respectively, denote the surfaces of the artificial and primary boundaries. In Figure 3.1, a spheroid is divided into two sub-particles and a cylinder into three sub-particles.

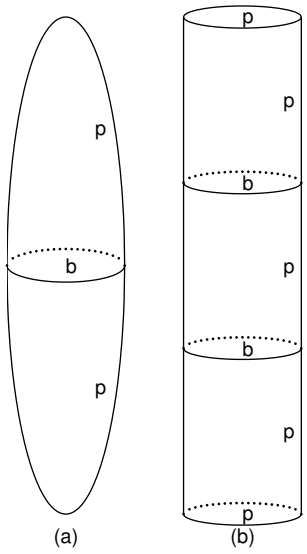

Figure 3.1: The schematic divisions of a spheroid and a cylinder. The spheroid is divided into two sub-particles and the cylinder into three sub-particles. The letters b and p respectively denote the surfaces for the artificial and primary boundaries of the original particle.

Using Eq.(3.3), we have the following equation for the N sub-particles [8, 2]:

$$\begin{pmatrix} p_{mn}^{(i)} \\ q_{mn}^{(i)} \end{pmatrix} = \sum_{m'n'} T_{mnm'n'}^{(i)} \begin{pmatrix} a_{m'n'}^{(i)} \\ b_{m'n'}^{(i)} \end{pmatrix}, i = 1, ..., N \tag{3.4}$$

where the index i enumerates the sub-particle and $T^{(i)}$ indicates the T-matrix of the i-th sub-particle. For clarity in the following derivations, a spheroid divided into two sub-particles is taken as a canonical problem, as shown in the left panel of Figure 3.1. The surface electromagnetic field of the two sub-particles can be formally expressed as:

$$(\mathbf{E}|\mathbf{H})_{s_1}(\vec{r}) = \begin{cases} (\mathbf{E}|\mathbf{H})_{1p}(\vec{r}) & \vec{r} \in s_{1p} \\ (\mathbf{E}|\mathbf{H})_{1b}(\vec{r}) = (\mathbf{E}|\mathbf{H})_2^{int}(\vec{r}) & \vec{r} \in s_{1b} \end{cases} \tag{3.5}$$

$$(\mathbf{E}|\mathbf{H})_{s_2}(\vec{r}) = \begin{cases} (\mathbf{E}|\mathbf{H})_{2p}(\vec{r}) & \vec{r} \in s_{2p} \\ (\mathbf{E}|\mathbf{H})_{2b}(\vec{r}) = (\mathbf{E}|\mathbf{H})_1^{int}(\vec{r}) & \vec{r} \in s_{2b} \end{cases} \tag{3.6}$$

Where s_1 and s_2 denote the surfaces of lower sub-particle and upper sub-particle and subscripts p and b denote the primary part and the artificial part of the surface. $\mathbf{E}_1^{int}(\vec{r})$ and $\mathbf{H}_1^{int}(\vec{r})$, $\mathbf{E}_2^{int}(\vec{r})$ and $\mathbf{H}_2^{int}(\vec{r})$ represent the internal electromagnetic fields of the lower and upper sub-particles. The physical meaning of the above set of equations are that the incident electromagnetic field of the sub-particle is composed of two parts: the primary surface part, which is the original incident electromagnetic field plus the scattered electromagnetic field from another sub-particle, and the artificial surface part, which is actually the internal electromagnetic field of the adjacent sub-particle.

The incident field and scattered field can both be expressed as surface integrals involving surface electromagnetic fields through the EBCM. Consequently, the ex-

pansion coefficients can be expressed as surface integrals involving the surface electromagnetic fields and vector spherical wave functions [2]. We first set the common reference frame of the original scatterer to coincide with that of the first sub-particle. The incident expansion coefficients of the original scatter can be expressed as [2]:

$$\begin{pmatrix} a_{mn}^{o(1)} \\ b_{mn}^{o(1)} \end{pmatrix} = (-)^m k \oint_s ds \left\{ \omega\mu_0[\hat{n} \times \mathbf{H}_p(\vec{r})] \begin{pmatrix} \mathbf{M}_{-mn}(k\vec{r}_1) \\ \mathbf{N}_{-mn}(k\vec{r}_1) \end{pmatrix} \right. \\ \left. -ik[\hat{n} \times \mathbf{E}_p(\vec{r})] \begin{pmatrix} \mathbf{N}_{-mn}(k\vec{r}_1) \\ \mathbf{M}_{-mn}(k\vec{r}_1) \end{pmatrix} \right\} \tag{3.7}$$

where the superscript $o(1)$ denotes the expansion coefficients of the original scatterer, whose reference frame coincides with that of the first sub-particle. $\hat{n}$ is the outward unit normal at the surface area of the original scatterer indicated by s. The surface integration can be divided into two parts based on the compositions of the surface: the primary surfaces of the lower and upper sub-particles. The integration $\oint_s ds$ can be divided as $(\int_{s_{1p}} ds_{1p} + \int_{s_{2p}} ds_{2p})$. Similarly, the incident expansion coefficients of the lower sub-particle are [2]:

$$\begin{pmatrix} a_{mn}^{(1)} \\ b_{mn}^{(1)} \end{pmatrix} = (-)^m k \oint_{s_1} ds_1 \left\{ \omega\mu_0[\hat{n} \times \mathbf{H}_{s_1}(\vec{r})] \begin{pmatrix} \mathbf{M}_{-mn}(k\vec{r}_1) \\ \mathbf{N}_{-mn}(k\vec{r}_1) \end{pmatrix} \right. \\ \left. -ik[\hat{n} \times \mathbf{E}_{s_1}(\vec{r})] \begin{pmatrix} \mathbf{N}_{-mn}(k\vec{r}_1) \\ \mathbf{M}_{-mn}(k\vec{r}_1) \end{pmatrix} \right\} \tag{3.8}$$

Likewise, the surface integration can be divided into two parts based on the compo-

sitions of the surface: the primary surface and the artificial surface:

$$\begin{pmatrix} a_{mn}^{(1)} \\ b_{mn}^{(1)} \end{pmatrix} = (-)^m k \int_{s_{1p}} ds_{1p} \left\{ \omega\mu_0[\hat{n} \times \mathbf{H}_{1p}(\vec{r})] \begin{pmatrix} \mathbf{M}_{-mn}(k\vec{r}_1) \\ \mathbf{N}_{-mn}(k\vec{r}_1) \end{pmatrix} \right.$$
$$\left. -ik[\hat{n} \times \mathbf{E}_{1p}(\vec{r})] \begin{pmatrix} \mathbf{N}_{-mn}(k\vec{r}_1) \\ \mathbf{M}_{-mn}(k\vec{r}_1) \end{pmatrix} \right\}$$
$$+(-)^m k \int_{s_{1b}} ds_{1b} \left\{ \omega\mu_0[\hat{n} \times \mathbf{H}_2^{int}(\vec{r})] \begin{pmatrix} \mathbf{M}_{-mn}(k\vec{r}_1) \\ \mathbf{N}_{-mn}(k\vec{r}_1) \end{pmatrix} \right.$$
$$\left. -ik[\hat{n} \times \mathbf{E}_2^{int}(\vec{r})] \begin{pmatrix} \mathbf{N}_{-mn}(k\vec{r}_1) \\ \mathbf{M}_{-mn}(k\vec{r}_1) \end{pmatrix} \right\} \tag{3.9}$$

where the above expression has already used the Eq.(3.5). For Eq.(3.9), the first term can be written as in terms of Eq.(3.7):

$$\begin{pmatrix} a_{mn}^{o(1)} \\ b_{mn}^{o(1)} \end{pmatrix} - (-)^m k \oint_{s_{2p}} ds_{2p} \left\{ \omega\mu_0[\hat{n} \times \mathbf{H}_{2p}(\vec{r})] \begin{pmatrix} \mathbf{M}_{-mn}(k\vec{r}_1) \\ \mathbf{N}_{-mn}(k\vec{r}_1) \end{pmatrix} \right.$$
$$\left. -ik[\hat{n} \times \mathbf{E}_{2p}(\vec{r})] \begin{pmatrix} \mathbf{N}_{-mn}(k\vec{r}_1) \\ \mathbf{M}_{-mn}(k\vec{r}_1) \end{pmatrix} \right\} \tag{3.10}$$

On the artificial surface, the boundary conditions are invoked:

$$\hat{n} \times \mathbf{H}_2^{int}(\vec{r}) = -\hat{n} \times \mathbf{H}_1^{int}(\vec{r}),\ \hat{n} \times \mathbf{E}_2^{int}(\vec{r}) = -\hat{n} \times \mathbf{E}_1^{int}(\vec{r}), \vec{r} \in s_{1b}||s_{2b} \tag{3.11}$$

The vector spherical wave functions are based on the frame of reference of the lower sub-particle in Eq.(3.9). They can be transformed into the functions based on the frame of reference of the upper sub-particle in terms of the addition theorem [61, 62,

63]:

$$\begin{pmatrix} \mathbf{M}_{-mn}(k\vec{r}_1) \\ \mathbf{N}_{-mn}(k\vec{r}_1) \end{pmatrix} = \sum_{n'=s}^{\infty} \begin{pmatrix} A_{-mn'}^{-mn}(k\vec{r}_{12}) & B_{-mn'}^{-mn}(k\vec{r}_{12}) \\ B_{-mn'}^{-mn}(k\vec{r}_{12}) & A_{-mn'}^{-mn}(k\vec{r}_{12}) \end{pmatrix} \begin{pmatrix} \mathbf{RgM}_{-mn'}(k\vec{r}_2) \\ \mathbf{RgN}_{-mn'}(k\vec{r}_2) \end{pmatrix} \quad (3.12)$$

where $s = \max(1, |m|)$ and $r_2 < r_{12}$. In Eq.(3.12), $\vec{r}_1 = \vec{r}_{12} + \vec{r}_2$ and $\vec{r}_{12}$ represents the displacement vector from the origin of the lower sub-particle to the origin of the upper sub-particle. The functions $A(k\vec{r}_{12})$ and $B(k\vec{r}_{12})$ are the translational coefficients from the addition theorem and the specific expressions are defined in [2]. Combining Eqs.(3.9-3.12), the incident expansion coefficients of the lower sub-particle can be transformed as:

$$\begin{pmatrix} a_{mn}^{(1)} \\ b_{mn}^{(1)} \end{pmatrix} = \begin{pmatrix} a_{mn}^{o(1)} \\ b_{mn}^{o(1)} \end{pmatrix} + \sum_{n'=s}^{\infty} \begin{pmatrix} A_{-mn'}^{-mn}(k\vec{r}_{12}) & B_{-mn'}^{-mn}(k\vec{r}_{12}) \\ B_{-mn'}^{-mn}(k\vec{r}_{12}) & A_{-mn'}^{-mn}(k\vec{r}_{12}) \end{pmatrix} \begin{pmatrix} p_{mn'}^{(2)} \\ q_{mn'}^{(2)} \end{pmatrix} \quad (3.13)$$

where the scattering expansion coefficients of the upper sub-particle are defined in [2]:

$$\begin{pmatrix} p_{mn'}^{(2)} \\ q_{mn'}^{(2)} \end{pmatrix} = (-)^m k \oint_{s_2} ds_2 \left\{ \omega\mu_0[\hat{n} \times \mathbf{H}_{s_2}(\vec{r})] \begin{pmatrix} \mathbf{RgM}_{-mn'}(k\vec{r}_2) \\ \mathbf{RgN}_{-mn'}(k\vec{r}_2) \end{pmatrix} \right.$$
$$\left. -ik[\hat{n} \times \mathbf{E}_{s_2}(\vec{r})] \begin{pmatrix} \mathbf{RgN}_{-mn'}(k\vec{r}_2) \\ \mathbf{RgM}_{-mn'}(k\vec{r}_2) \end{pmatrix} \right\} \quad (3.14)$$

Similarly, the relation can be given when the common reference frame of the original scatterer coincides with that of the second sub-particle. Furthermore, we can

generalize the expression for the number of sub-particles from 2 to N as:

$$\begin{pmatrix} a_{mn}^{(i)} \\ b_{mn}^{(i)} \end{pmatrix} = \begin{pmatrix} a_{mn}^{o(i)} \\ b_{mn}^{o(i)} \end{pmatrix} + \sum_{\substack{j=1 \\ j\neq i}}^{N} \sum_{n'=s}^{\infty} \begin{pmatrix} A_{-mn'}^{-mn}(k\vec{r}_{ij}) & B_{-mn'}^{-mn}(k\vec{r}_{ij}) \\ B_{-mn'}^{-mn}(k\vec{r}_{ij}) & A_{-mn'}^{-mn}(k\vec{r}_{ij}) \end{pmatrix} \begin{pmatrix} p_{mn'}^{(j)} \\ q_{mn'}^{(j)} \end{pmatrix} \quad (3.15)$$

where $i = 1, ..., N$. The superscript $o(i)$ denotes the expansion coefficients of the original scatterer, whose reference frame coincides with the one of the i-th sub-particle, and $\vec{r}_{ij}$ represents the displacement vector from the origin of the i-th sub-particle to the one of the j-th sub-particle. There are similar derivations in [8].

Eq.(3.15) has a physical meaning similar to many-body scattering problems. The incident field of the i-th sub-particle is composed of the original incident field, the scattered field from other sub-particles, and the internal field from adjacent sub-particles in this situation while the original incident field and the scattered field from other particles are used for the many-body problems. That is the reason that the expansion coefficients include the contribution of the artificial boundary part. When the sub-particles are separated in the axial direction to the extent that the smallest circumscribed spheres of the particles do not intersect, the contribution of the artificial boundary part disappears and Eq.(3.15) returns exactly to the expressions of axial many body scattering. In Eq.(3.15), all of the coefficients are decoupled with a different m due to axial translations among the sub-particles. In the case of non-axial translations, translational coefficients are coupled with different m-components. In order to decouple addition coefficients from different m-components, an efficient algorithm introduced by Fuller and Mackowski [64] is employed. We assume the non-axial translation in Eq.(3.15) to be implemented from the reference frames of the i-th sub-particle to the j-th sub-particle. The translation can be decomposed into three steps: a coordinate rotation from the i-th reference frame toward the j-th

frame; an axial translation; and, an inverse coordinate rotation of the i-th reference frame [64].

In Eqs.(3.4) and (3.15), an iterative technique [10, 11, 12] is employed to calculate the expansion coefficients by assuming the initial values of the incident expansion coefficients of sub-particles are equal to the original incident expansion coefficients, that is, $a_{mn}^{(i)} = a_{mn}^{o(i)}$ and $b_{mn}^{(i)} = b_{mn}^{o(i)}$. After the sub-particles expansion coefficients are obtained by the iterative technique, the expansion coefficients of the original scatterer can be calculated using the addition theorem:

$$\begin{pmatrix} p_{mn}^{o(i)} \\ q_{mn}^{o(i)} \end{pmatrix} = \begin{pmatrix} p_{mn}^{(i)} \\ q_{mn}^{(i)} \end{pmatrix} + \sum_{\substack{j=1 \\ j\neq i}}^{N} \sum_{n'=s}^{\infty} \begin{pmatrix} RgA_{-mn'}^{-mn}(k\vec{r}_{ij}) & RgB_{-mn'}^{-mn}(k\vec{r}_{ij}) \\ RgB_{-mn'}^{-mn}(k\vec{r}_{ij}) & RgA_{-mn'}^{-mn}(k\vec{r}_{ij}) \end{pmatrix} \begin{pmatrix} p_{mn'}^{(j)} \\ q_{mn'}^{(j)} \end{pmatrix} \quad (3.16)$$

where the functions $RgA(k\vec{r}_{ij})$ and $RgB(k\vec{r}_{ij})$ are translational coefficients, whose expressions can be found in [2], and the other notations are consistent with previous ones. In Eq.(3.16), a different $o(i)$ represents a different reference frame for the original scatterer; however, the choice of origins is independent of the scattering properties of particles. Thus, we can make the common reference frame coincide with that of the first sub-particle. Eqs.(3.15) and (3.16) are similar to the two equations for the case of multiple cylinders found in [60].

From Eqs.(3.15) and (3.16), a transitional matrix connecting the original scattering expansion coefficients and incident expansion coefficients relative to the same reference frame can be obtained. In this study, we focus on the iterative algorithm, and a simpler way than Eq.(3.16) is employed to express the scattering expansion coefficients of the original scatterer. In the far field, Eq.(3.2) can be simplified as:

$$\mathbf{E}^{sca}(k\vec{r})|_{kr\to\infty} = \frac{exp(ikr)}{-ikr} \sum_{mn} (-i)^{n+1} \left\{ p_{mn} \left[\mathbf{A}_{mn}(\theta,\varphi)/i \right] + q_{mn} \left[\mathbf{B}_{mn}(\theta,\varphi) \right] \right\} \quad (3.17)$$

where Eqs.(2.28) and (2.29) have been used and (r, θ, ϕ) are the field point coordinates in spherical coordinates. When the origin of the reference frame translates from point 1 to point 2, the same field point coordinates of the two reference frames in the far field approximations can be formulated as:

$$\theta_1 = \theta_2, \varphi_1 = \varphi_2, r_1 = \sqrt{|\vec{r}_{12} + \vec{r}_2|^2} \approx r_2 + \vec{r}_{12} \cdot \frac{\vec{r}_2}{r_2} \tag{3.18}$$

where $\vec{r}_2/r_2 = \vec{r}_1/r_1 = \hat{k}_s$ is the unit vector of the field point direction. At the same point, the value of the electric field is independent of the choices of the origin. Through Eq.(3.17), the scattering expansion coefficients of the two reference frames have the relation:

$$\begin{pmatrix} p_{mn}^{(2)} \\ q_{mn}^{(2)} \end{pmatrix} = \begin{pmatrix} p_{mn}^{(1)} \\ q_{mn}^{(1)} \end{pmatrix} exp(i\vec{k}_s \cdot \vec{r}_{12}) \tag{3.19}$$

Consequently, the scattering expansion coefficients of the original scatterer, whose common reference frame coincides with that of the first sub-particle, can be expressed in terms of the expansion coefficients of the sub-particles:

$$\begin{pmatrix} p_{mn}^{o(1)} \\ q_{mn}^{o(1)} \end{pmatrix} = \begin{pmatrix} p_{mn}^{(1)} \\ q_{mn}^{(1)} \end{pmatrix} + \sum_{j=2}^{N} \begin{pmatrix} p_{mn}^{(j)} \\ q_{mn}^{(j)} \end{pmatrix} exp(-i\vec{k}_s \cdot \vec{r}_{1j}) \tag{3.20}$$

Eq.(3.20) is substituted for Eq.(3.16) in the MBIT method.

3.3 Simulation results and discussion

Three codes, T-matrix [65, 35], ADDA [66], and MSTM [67], are chosen as benchmarks to compare the simulation results with those calculated by the MBIT code, in which the transition matrix of each sub-particle in Eq.(3.4) is calculated using the T-matrix code. Normally, two methods are used to express the amplitude matrix

that connects the scattered electric field with the incident electric field; the first is with respect to the meridional planes of the scattered and the incident directions [2]:

$$\begin{pmatrix} E_\theta^{sca} \\ E_\varphi^{sca} \end{pmatrix} = \frac{exp(ikr)}{-ikr} \begin{pmatrix} s_{11}^m & s_{12}^m \\ s_{21}^m & s_{22}^m \end{pmatrix} \begin{pmatrix} E_\theta^{int} \\ E_\varphi^{int} \end{pmatrix} \tag{3.21}$$

Due to the linearity of Eq.(3.21), the amplitude scattering matrix can be obtained by setting the incident doublets, $(E_\theta^{int}, E_\varphi^{int})$, as (1,0) and (0,1), respectively. In terms of Eqs.(2.28), (2.29) and (3.17), the amplitude scattering matrix can consequently be formulated as follows:

$$s_{11}^m = \sum_{n=1}^{\infty} \sum_{m=-n}^{n} (-i)^{n+1}(-1)^m \gamma_n \exp(im\varphi) \left[\pi_{mn}(\theta) p_{mn}^1 + \tau_{mn}(\theta) q_{mn}^1\right] \tag{3.22}$$

$$s_{21}^m = \sum_{n=1}^{\infty} \sum_{m=-n}^{n} (-i)^{n}(-1)^m \gamma_n \exp(im\varphi) \left[\tau_{mn}(\theta) p_{mn}^1 + \pi_{mn}(\theta) q_{mn}^1\right] \tag{3.23}$$

$$s_{12}^m = \sum_{n=1}^{\infty} \sum_{m=-n}^{n} (-i)^{n+1}(-1)^m \gamma_n \exp(im\varphi) \left[\pi_{mn}(\theta) p_{mn}^2 + \tau_{mn}(\theta) q_{mn}^2\right] \tag{3.24}$$

$$s_{22}^m = \sum_{n=1}^{\infty} \sum_{m=-n}^{n} (-i)^{n}(-1)^m \gamma_n \exp(im\varphi) \left[\tau_{mn}(\theta) p_{mn}^2 + \pi_{mn}(\theta) q_{mn}^2\right] \tag{3.25}$$

where $\gamma_n = \sqrt{\frac{2n+1}{4\pi n(n+1)}}$, π and τ have been defined in Eqs.(2.32), (2.33) and (2.34), and the superscript 1 and 2 represent the corresponding expansion coefficients of the scattered field associated with the incident doublets (1,0) and (0,1), respectively.

The second one expressing the amplitude scattering matrix is with respect to the scattering plane containing both the incident and scattering directions [22, 23]:

$$\begin{pmatrix} E_\parallel^{sca} \\ E_\perp^{sca} \end{pmatrix} = \frac{exp(ikr)}{-ikr} \begin{pmatrix} s_{11} & s_{12} \\ s_{21} & s_{22} \end{pmatrix} \begin{pmatrix} E_\parallel^{int} \\ E_\perp^{int} \end{pmatrix} \tag{3.26}$$

In this study, the incident direction is fixed and the scattering properties in different scattering directions are calculated with an iterative algorithm. The amplitude matrix is straightforward to calculate in terms of the respective meridional planes of scattering and incident directions. Most scattering studies present the scattering properties with respect to the scattering plane, which is equivalent to expressing the scattering properties in the incident reference frame. Consequently, a transformation between two amplitude matrices can be formulated as:

$$\begin{pmatrix} s_{11} & s_{12} \\ s_{21} & s_{22} \end{pmatrix} = \begin{pmatrix} -\hat{n}_\perp \cdot \hat{n}_\varphi^{(s)} & \hat{n}_\perp \cdot \hat{n}_\theta^{(s)} \\ \hat{n}_\perp \cdot \hat{n}_\theta^{(s)} & \hat{n}_\perp \cdot \hat{n}_\varphi^{(s)} \end{pmatrix} \begin{pmatrix} s_{11}^m & s_{12}^m \\ s_{21}^m & s_{22}^m \end{pmatrix} \begin{pmatrix} -\hat{n}_\varphi^{(i)} \cdot \hat{n}_\perp & \hat{n}_\theta^{(i)} \cdot \hat{n}_\perp \\ \hat{n}_\theta^{(i)} \cdot \hat{n}_\perp & \hat{n}_\varphi^{(i)} \cdot \hat{n}_\perp \end{pmatrix} \tag{3.27}$$

$$\hat{n}_\theta^{(s)|(i)} \times \hat{n}_\varphi^{(s)|(i)} = \hat{n}_\perp \times \hat{n}_\parallel^{(s)|(i)} = \hat{n}^{(s)|(i)} \tag{3.28}$$

where $\hat{n}_\theta$ and $\hat{n}_\varphi$ denote the unit vectors of the zenithal and azimuthal directions with respect to the meridional plane, $\hat{n}_\perp$ and $\hat{n}_\parallel$ denote the unit vectors perpendicular and parallel to the scattering plane, and $\hat{n}^{(s)}$ and $\hat{n}^{(i)}$ denote the unit vectors of the scattering and incident directions. We assume the incident direction (θ_i, φ_i) is relative to the laboratory reference frame. The scattering direction (θ, φ), relative to the incident reference frame, can be transformed into the scattering direction (θ_s, φ_s) relative to the laboratory reference frame:

$$\begin{cases} \cos\theta_s = -\sin\theta_i \sin\theta \cos\varphi + \cos\theta_i \cos\theta \\ \cos\varphi_s = \frac{\cos\theta_i \cos\varphi_i \sin\theta \cos\varphi - \sin\varphi_i \sin\theta \sin\varphi + \sin\theta_i \cos\varphi_i \cos\theta}{\sin\theta_s} \\ \sin\varphi_s = \frac{\cos\theta_i \sin\varphi_i \sin\theta \cos\varphi + \cos\varphi_i \sin\theta \sin\varphi + \sin\theta_i \sin\varphi_i \cos\theta}{\sin\theta_s} \end{cases} \tag{3.29}$$

The matrix elements in the transformation of Eq.(3.27) are:

$$\hat{n}_{\perp} \cdot \hat{n}_{\theta}^{(s)} = -\cos\theta_i \sin\varphi \cos\theta_s \cos(\varphi_s - \varphi_i) + \cos\varphi \cos\theta_s \sin(\varphi_s - \varphi_i) - \sin\theta_i \sin\varphi \sin\theta_s \tag{3.30}$$

$$\hat{n}_{\perp} \cdot \hat{n}_{\varphi}^{(s)} = \cos\theta_i \sin\varphi \sin(\varphi_s - \varphi_i) + \cos\varphi \cos(\varphi_s - \varphi_i) \tag{3.31}$$

$$\hat{n}_{\perp} \cdot \hat{n}_{\theta}^{(i)} = -\sin\varphi \tag{3.32}$$

$$\hat{n}_{\perp} \cdot \hat{n}_{\varphi}^{(i)} = \cos\varphi \tag{3.33}$$

In terms of Eqs.(3.27-3.33), we obtain the amplitude scattering matrix related to the scattering planes from the matrix related to the meridional planes. The Mueller matrix can be obtained in terms of Eqs.(2.10-2.25). The following subsections describe the simulation results of the Mueller matrix elements of different types of particles relative to the incident frame of reference.

3.3.1 Simulation results of many particles

Figure 3.2 shows the Mueller matrix elements of three cylinders calculated by the MBIT in comparison to those calculated with the ADDA. The diameter and height of each cylinder are 10 and 90 (note, hereafter physical lengths are specified in units of $\lambda/2\pi$, where λ is the incident wavelength in a vacuum) and the refractive index relative to the surrounding medium is 1.1+i0.0. The configuration of three cylinders is shown in the figure, and the incident direction and the rotational axes of the three cylinders are in the same plane. The angle between the rotational axes and the incident direction is 60^0. The distance between the centers of neighboring cylinders is 30. If the three cylinders were not divided, their smallest circumscribed spheres would intersect, and are shown in the figure. However, when each cylinder is divided into three identical sub-cylinders, the smallest circumscribed spheres of the sub-cylinders

do not intersect except with those associated with the original cylinder. Both the axial and non-axial translations between the sub-particles reference frames are involved in practical calculations. Moreover, the circumscribed spheres between the sub-particles with non-axial reference frames do not intersect. The Mueller matrix elements of the configuration relative to the incident reference frame are shown. The abscissae from 0^0 to 180^0 represent the zenith scattering directions and the scattering properties are averaged in the azimuthal directions. The results calculated using the MBIT are perfectly consistent with the ADDA calculated benchmark results.

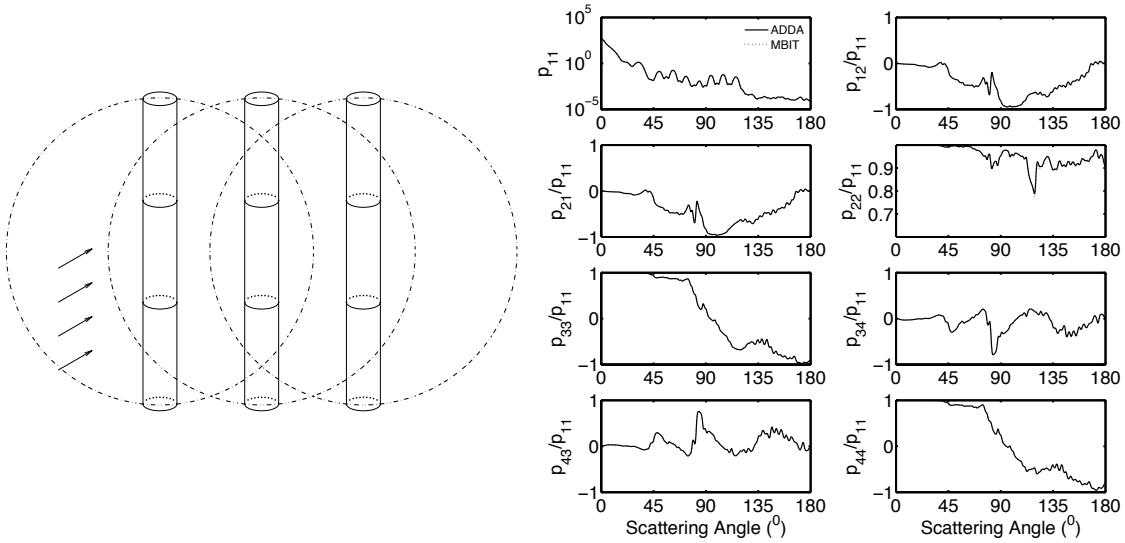

Figure 3.2: The Mueller matrix elements of three cylinders calculated by the MBIT in comparison to those calculated with the ADDA.

Figure 3.3 shows the Mueller matrix elements of two identical prolate spheroids calculated by the MBIT in comparison to those calculated with the ADDA. The configuration of the two spheroids is shown in the figure, and the incident direction is perpendicular to the rotational axes. The semi-major and semi-minor axes of

each spheroid are 40 and 10, respectively, and the refractive index is 1.2+i0.001. The two-spheroid configuration possesses the rotationally invariant property. The configuration of the Mueller matrix is the same as in Figure 3.2. As shown in the figure, the MBIT is applicable to many-particle systems for which the circumscribed spheres of the sub-particles do not intersect.

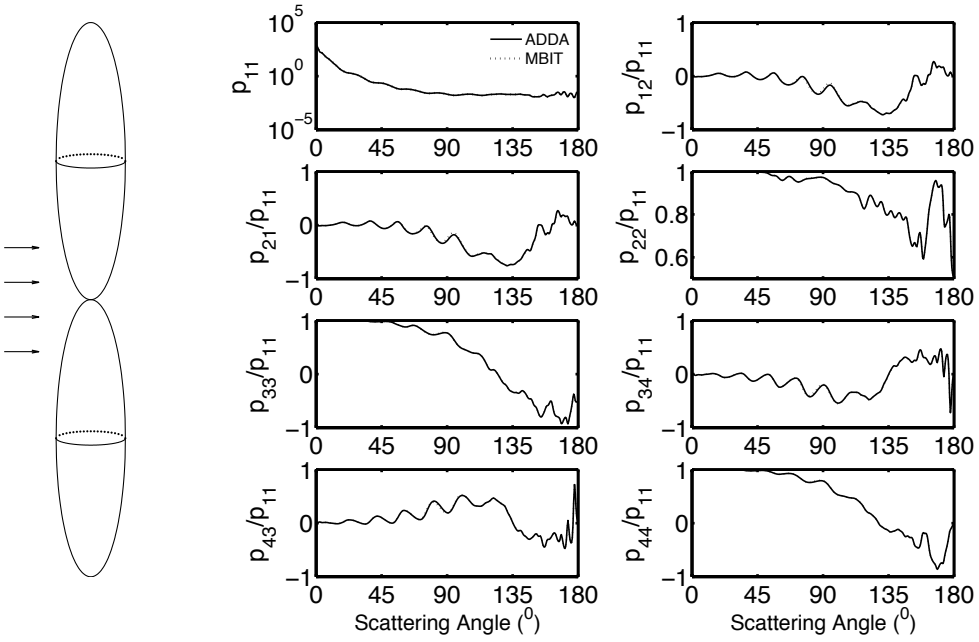

Figure 3.3: Mueller matrix elements of two spheroids calculated by the MBIT in comparison to those calculated with the ADDA.

Figure 3.4 shows the Mueller matrix elements of an aggregate composed of one spheroid and one sphere calculated by the MBIT in comparison to those calculated with the ADDA. The figure shows the configuration, in which the rotational axes of the two particles are in the same line and the angle between the incident direction and the line is 60^0. The semi-major and semi-minor axes of the spheroid are 40

and 10, respectively, and the refractive index is 1.1+i0.0. The radius of the sphere is 15 and the refractive index is 1.2+i0.0. The distance between the centers of the spheroid and the sphere is 60. The configuration of the Mueller matrix is the same as in Figure 3.2. As shown in the figure, the agreement between the MBIT and the ADDA results further validates the applicability of the method to solve the normal many-body scattering problem.

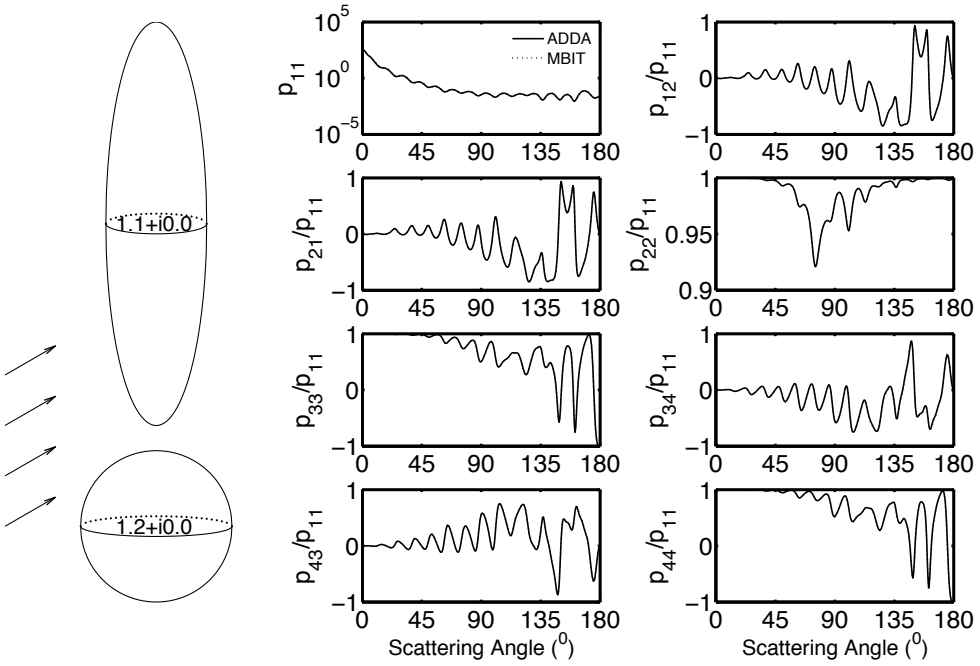

Figure 3.4: Mueller matrix elements of one spheroid and one sphere calculated by the MBIT in comparison to those calculated with the ADDA.

Figure 3.5 shows the Mueller matrix elements of two separated spheres with different refractive indices calculated by the MBIT in comparison to those calculated with the MSTM. The configuration of two spheres is shown inside the p_{11} panel, where the centers of the two spheres and the incident direction are in the x-z plane

of the laboratory reference frame. The first sphere is centered at (0,0,0), the radius is 30, and the corresponding refractive index is 1.1+i0.0. The second sphere is centered at (60,0,60), the radius is 20, and the corresponding refractive index is 1.2+i0.0. The incident zenithal and azimuthal angles relative to the laboratory frame are (60^0,0^0). The figure shows the scattering properties in one single scattering plane, which has a 54^0 angle with the x-axis of the incident reference frame, and is in the zenithal direction from 0^0 to 180^0. The comparison results show a perfect match between the MBIT and the MSTM methods.

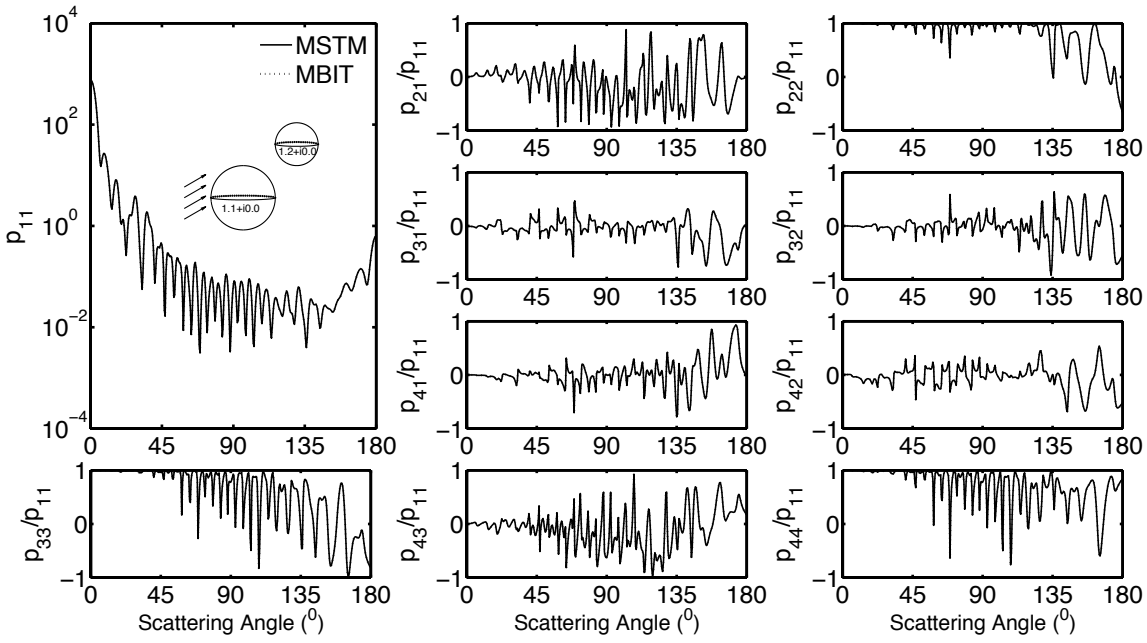

Figure 3.5: Mueller matrix elements of two spheres calculated by the MBIT in comparison to those calculated with the MSTM.

3.3.2 Simulation results of a single particle

Figure 3.6 shows the Mueller matrix elements of a homogeneous prolate cylinder with an extremely large aspect ratio calculated by the MBIT in comparison to those calculated with the ADDA. The cylinder configuration, in which the incident direction is perpendicular to the end surfaces, is shown inside the p_{11} panel. The diameter and height of the cylinder are 10 and 180 and the refractive index is 1.2+i0.001. For this calculation, the cylinder is divided into six identical sub-cylinders. The abscissae from 0^0 to 180^0 is the scattering direction relative to the incident direction and the scattering matrix is independent of the azimuthal direction. As shown in the figure, the acute spikes have a few differences. For the end-on incidence, the electromagnetic fields will have strong interference, which cause the numerous oscillations in the phase function. Due to the limits of computational precision, some slight errors may appear in the spikes. Figure 3.7 shows the Mueller matrix elements of a prolate spheroid calculated by the MBIT in comparison to those calculated with the T-matrix. The spheroid configuration, in which the incident direction is perpendicular to the cross section, is shown inside the p_{11} panel. The semi-major and semi-minor axes are 50 and 10, respectively, and the refractive index is 1.05+i0.0. As shown in the figure, the spheroid is divided into two sub-particles in the practical calculations. The abscissae from 0^0 to 180^0 are the scattering directions relative to the incident direction and the scattering matrix is independent of the azimuthal directions. In the figure, the simulation results have some small discrepancies compared with those calculated with the T-matrix for the elements p_{12}/p_{11} and p_{34}/p_{11} in the backscattering direction. The reason for the discrepancy will require further study. Figure 3.8 shows the Mueller matrix elements of an inhomogeneous prolate cylinder calculated by the MBIT in comparison to those calculated with the ADDA. The cylinder

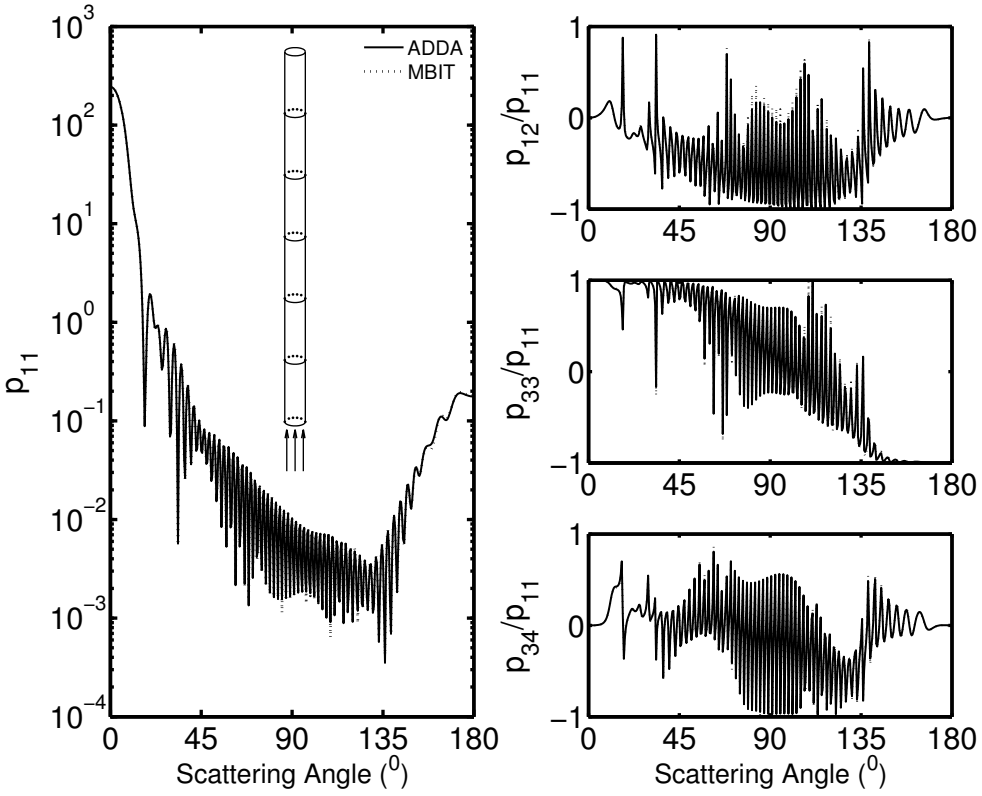

Figure 3.6: Mueller matrix elements of a single cylinder calculated by the MBIT in comparison to those calculated with the ADDA.

configuration is shown in the figure, and the angle between the rotational axis of the cylinder and the incident direction is 60^0 and the refractive indices relative to the surrounding medium of the sub-cylinders are marked. The diameter and height of the cylinder are 10 and 90. In the calculation, the cylinder is divided into three sub-cylinders with identical sizes but different refractive indices. The configuration of the Mueller matrix is the same as in Figure 3.2. The two results from the MBIT and the ADDA are again in good agreement. Figure 3.9 shows the Mueller matrix elements of a compound particle with a half spheroid and a half cylinder calculated

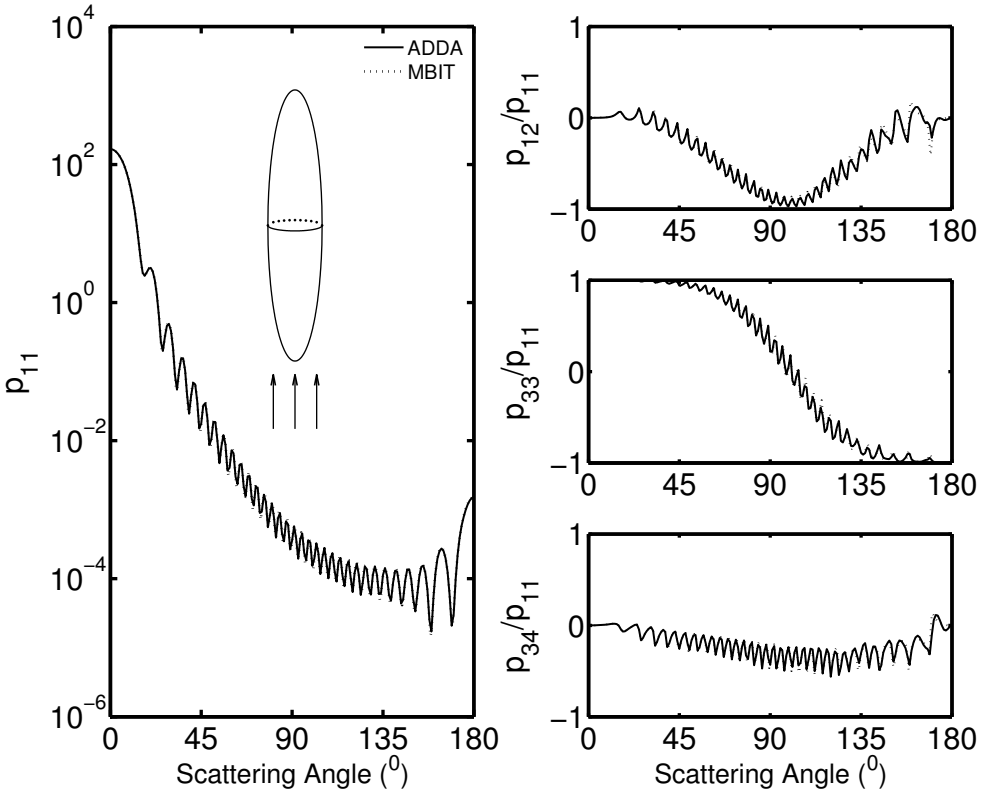

Figure 3.7: Mueller matrix elements of a single spheroid calculated by the MBIT in comparison to those calculated with the T-Matrix.

by the MBIT in comparison to those calculated with the ADDA. The compound particle configuration is shown in the figure, and the angle between the rotational axis of the particle and the incident direction is 60^0 and the refractive indices relative to the surrounding medium of the sub-cylinders are marked. The upper half of the particle is a half spheroid with semi-major and semi-minor axes of 50 and 10, respectively. The refractive index relative to the surrounding medium is 1.1+i0.0. The lower half of the particle is a cylinder with a diameter and height of 20 and 40. The refractive index relative to the surrounding medium is 1.2+i0.0. The configuration

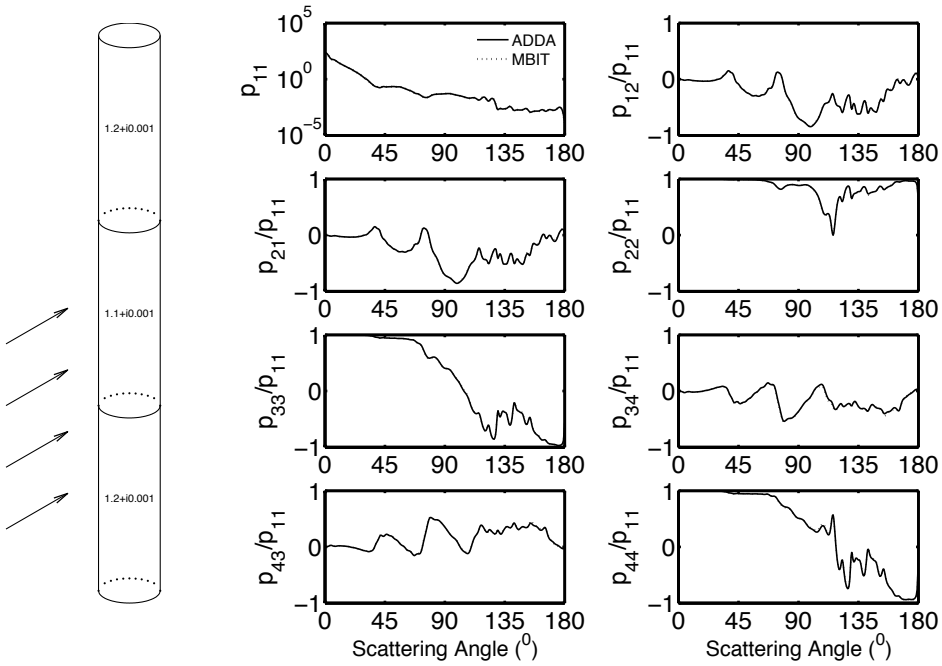

Figure 3.8: Mueller matrix elements of an inhomogeneous cylinder calculated by the MBIT in comparison to those calculated with the ADDA.

of the Mueller matrix is the same as in Figure 3.2. The comparisons show excellent agreement between the MBIT and the benchmark method.

3.4 Conclusion

A new iterative method based on the T-matrix method is employed to calculate the scattering properties of composite particles and particles with large aspect ratios. The original particle is divided into several sub-particles and the scattering of each sub-particle is calculated using the T-matrix method. The scattering properties of the original particle are obtained in terms of a series of iterative equations of the sub-particles scattering. The results computed from the iterative method agree well with those from the conventional T-matrix (EBCM), ADDA, and MSTM methods.

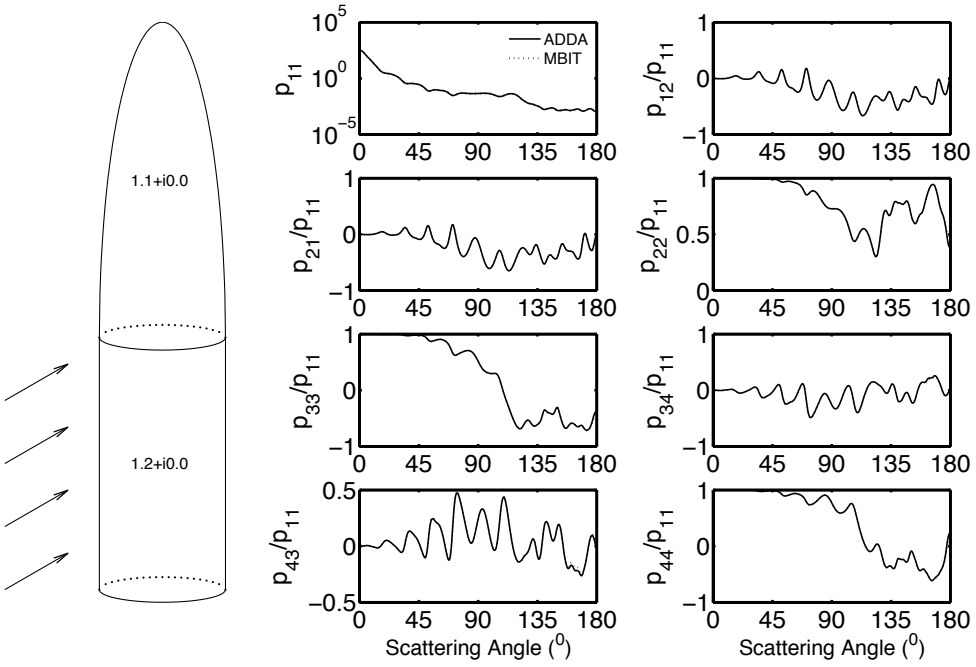

Figure 3.9: Mueller matrix elements of a combined particle with a half spheroid and a half cylinder calculated by the MBIT in comparison to those calculated with the ADDA.

4. SCATTERING OF 1-D PERIODIC SCATTERER AND ASYMPTOTIC COMPARISON USING THE MBIT METHOD*

4.1 Introduction

The single-scattering properties of finite non-spherical scatterers with small size parameters can be solved by numerically accurate methods, such as the finite-difference time domain (FDTD) method [29, 30, 44], the discrete dipole approximation (DDA) method [31, 45, 46], and the pseudo-spectral time domain (PSTD) method [32, 47, 48]. They can also be obtained by using the extended boundary condition method (EBCM) [4, 5, 2] and invariant imbedding T-matrix (II-TM) method [6, 7]. These methods can generally be applied to scatterers with size parameters up to approximately 100. For scatterers with axial rotational symmetry, the EBCM and II-TM can be applied up to size parameters of 200. However, the EBCM has been reported to have ill-conditioned problems for scatterers with high aspect ratios [68]. Several methods are developed in order to obtain the single scattering by scatterers with high aspect ratios (e.g. null-field method with discrete sources [59], many-body iterative T-matrix method (MBIT) [8, 9] and iterative EBCM (IEBCM) [69, 70, 71]. The iteration and division of scatterers techniques are employed by both the MBIT and the IEBCM; however, the MBIT uses boundary conditions of adjacent sub-scatterers whereas the IEBCM uses a point-matching method to establish the relationships of different sub-scatterers.

In the case of the scattering of light by an infinite right circular cylinder, an accurate solution can be obtained [22, 23], which can be used to estimate light scattering

*Reprinted with permission from "Scattering of 1-D periodic scatterer and asymptotic comparison using the many-body iterative T-matrix method" by B. Sun, P. Yang, G. W. Kattawar and L. Bi. J. Quant. Spectrosc. Radiat. Transfer, **146**, 459-467. Copyright 2014 @Elsevier.

by a finite cylinder [72]. For a scatterer with a periodic structure, a numerically accurate solution can be obtained with the DDA method [73, 19]. In the literature, the scattering of periodic arrays of particles is discussed by Waterman and Pedersen [74] using the T-matrix method. In this study, a semi-analytical solution based on the MBIT [8, 9] will be presented for scatterers with a 1-D periodic structure.

Although scatterers with infinite size do not exist in reality, the scattering properties of scatterers with large aspect ratios may be replaced with the properties of infinite scatterers. In the literature, the optical properties of ice crystals and marine diatoms have been extensively reported (e.g.[75, 76, 77]). Many atmospheric and oceanic observations show the existence of scatterers with large aspect ratios (e.g., [17, 78]). If the aspect ratios of these particles are large, the scattering properties can be characterized by infinite long scatterers, and the preliminary results of this study indicate the scattering properties of finite scatterers with large aspect ratios can be approximately represented by those of their infinite counterparts.

This section is organized into six parts. A detailed theoretical derivation will be given in 4.2 and 4.3. A brief explanation for the extension of the MBIT from scatterers with axial rotational symmetry to those without will be at the end of 4.3. 4.4 will show validations in terms of the analytical solution of an infinite cylinder and the DDA method with periodic boundary conditions. In 4.5, a preliminary asymptotic comparison of cylinders and hexagonal scatterers will be described. The study conclusions are in 4.6.

4.2 The MBIT method in a 1-D periodic scatterer

For finite scatterers, incident and scattered electric fields can be expanded in terms of vector spherical wave functions [2]:

$$\mathbf{E}^{inc}(k\vec{r}) = \sum_{n=1}^{\infty} \sum_{m=-n}^{n} \left[a_{mn} \mathbf{RgM}_{mn}(k\vec{r}) + b_{mn} \mathbf{RgN}_{mn}(k\vec{r}) \right] \tag{4.1}$$

$$\mathbf{E}^{sca}(k\vec{r}) = \sum_{n=1}^{\infty} \sum_{m=-n}^{n} \left[p_{mn} \mathbf{M}_{mn}(k\vec{r}) + q_{mn} \mathbf{N}_{mn}(k\vec{r}) \right], \; r > r_{>} \tag{4.2}$$

where $r_{>}$ represents the radius of the smallest circumscribed sphere of the scatterer; **RgM** and **RgN** are the regular vector spherical wave functions, which are finite at the origin; **M** and **N** are the outgoing wave functions, which characterize radiating waves in the far field region; a_{mn} and b_{mn} are expansion coefficients for the incident field; and, p_{mn} and $q_{mn}$are expansion coefficients for the scattered field. According to the MBIT method, a scatterer with a large aspect ratio is divided into several sub-scatterers; and, the expansion coefficients for the incident and scattered fields associated with the scatterer can be represented by the ones associated with the sub-scatterers. Consequently, a 1-D periodic scatterer can be divided into an infinite number of identical sub-scatterers. Figure 4.1 is the schematic diagram showing several scatterers with periodic structure, where (a) is an infinite cylinder, (b) discrete periodic cylinders, and (c) an infinite hexagonal prism. For continuous scatterers, such as an infinite cylinder and a hexagonal prism, the sub-scatterer may have the same cross section but different aspect ratios. The origins of the frame of references are always located at the centers of the sub-scatterers; however, for infinite scatterers, there are an infinite number of options. These sub-scatterers are enumerated as continuous integers from minus to plus infinity, that is, $(-\infty, ..., -1, 0, 1, ..., +\infty)$. Suppose $a_{mn}^{(i)}$ and $b_{mn}^{(i)}$, $p_{mn}^{(i)}$ and $q_{mn}^{(i)}$, are the expansion coefficients for the incident

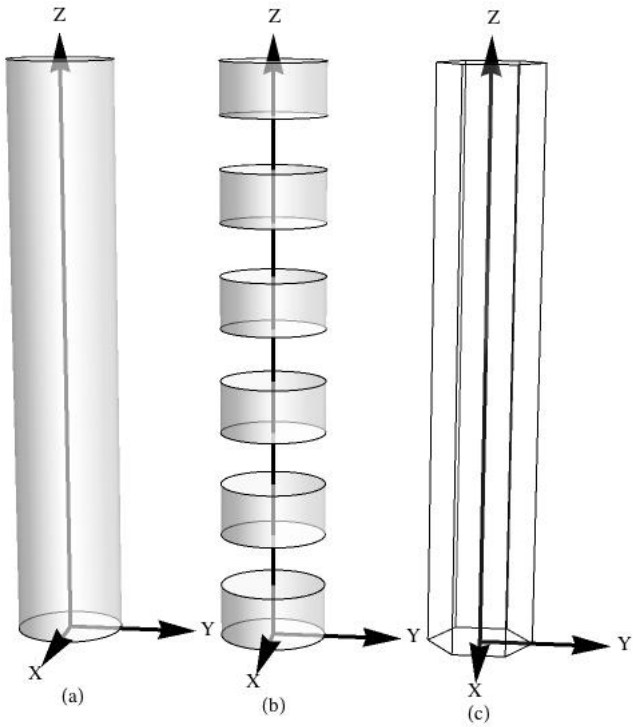

Figure 4.1: The schematic scatterers with 1-D periodic structure. (a) is an infinite cylinder; (b) are discrete periodic cylinders, where only 6 units are displayed; (c) is an infinite hexagonal prism. The origins of frame of references are always located in the center of scatterers. In this figure, the origins are situated at the bottom surface only for clarity.

field and scattered field of the i-th sub-scatterer, $a_{mn}^{o(i)}$ and $b_{mn}^{o(i)}$, $p_{mn}^{o(i)}$ and $q_{mn}^{o(i)}$, are the expansion coefficients of the 1-D periodic scatterer relative to the frame of reference of the i-th sub-scatter. In terms of the MBIT method [8, 9], the relationship of the

series of expansion coefficients can be represented as:

$$\begin{pmatrix} a_{mn}^{(i)} \\ b_{mn}^{(i)} \end{pmatrix} = \begin{pmatrix} a_{mn}^{o(i)} \\ b_{mn}^{o(i)} \end{pmatrix} + \sum_{\substack{j=-\infty \\ j\neq i}}^{\infty} \sum_{n'=s}^{\infty} \begin{pmatrix} A_{-mn'}^{-mn}(k\vec{r}_{ij}) & B_{-mn'}^{-mn}(k\vec{r}_{ij}) \\ B_{-mn'}^{-mn}(k\vec{r}_{ij}) & A_{-mn'}^{-mn}(k\vec{r}_{ij}) \end{pmatrix} \begin{pmatrix} p_{mn'}^{(j)} \\ q_{mn'}^{(j)} \end{pmatrix} \quad (4.3)$$

$$\begin{pmatrix} p_{mn}^{o(i)} \\ q_{mn}^{o(i)} \end{pmatrix} = \begin{pmatrix} p_{mn}^{(i)} \\ q_{mn}^{(i)} \end{pmatrix} + \sum_{\substack{j=-\infty \\ j\neq i}}^{\infty} \sum_{n'=s}^{\infty} \begin{pmatrix} RgA_{-mn'}^{-mn}(k\vec{r}_{ij}) & RgB_{-mn'}^{-mn}(k\vec{r}_{ij}) \\ RgB_{-mn'}^{-mn}(k\vec{r}_{ij}) & RgA_{-mn'}^{-mn}(k\vec{r}_{ij}) \end{pmatrix} \begin{pmatrix} p_{mn'}^{(j)} \\ q_{mn'}^{(j)} \end{pmatrix} \quad (4.4)$$

where $i = -\infty, ..., \infty$ and $s = \max(1, |m|)$; $\vec{r}_{ij}$ represents the displacement vector from the origin of the i-th frame of reference to the one of the j-th frame of reference, and A, B, RgA, and, RgB are axial translation coefficients [61, 62, 63, 13, 14, 79]. Due to sub-scatter equivalence, i=0 can be taken without loss of generality in the following discussion.

4.3 Semi-Analytical solution of 1-D periodic scatterer

In the far field, the scattered field of the j-th sub-scatterer can be formally expressed as:

$$\mathbf{E}^{sca}(k\vec{r}_j)|_{kr\to\infty} = \frac{exp(ikr_j)}{kr_j} \sum_{mn} \left[p_{mn}^{(j)} \mathbf{A}_{mn}^{(p)}(\theta, \varphi) + q_{mn}^{(j)} \mathbf{A}_{mn}^{(q)}(\theta, \varphi) \right] \quad (4.5)$$

where $\mathbf{A}^{(p)}(\theta, \varphi)$ and $\mathbf{A}^{(q)}(\theta, \varphi)$ are general functions of the scattering angles (θ, φ) . The phase of scattered field of the j-th sub-scatterer in the far field can be expanded as [19]:

$$kr_j = k|\vec{r}_0 - \vec{r}_{0j}| \approx kr_0 - \vec{k}_s \cdot \vec{r}_{0j} + \frac{1}{2kr_0} \left[(kr_0)^2 - (\vec{k}_s \cdot \vec{r}_{0j})^2 \right] \quad (4.6)$$

where r_0, r_j, and, r_{0j} represent radial coordinates relative to the 0-th and j-th frame of reference and the distance between the two origins, respectively; and, $\vec{k}_s = k\vec{r}_0/r_0$

is the scattered wave vector.

In terms of Eqs.(4.5) and (4.6), Eq.(4.4) can be replaced by a simplified version [9]:

$$\begin{pmatrix} p_{mn}^{o(0)} \\ q_{mn}^{o(0)} \end{pmatrix} = \begin{pmatrix} p_{mn}^{(0)} \\ q_{mn}^{(0)} \end{pmatrix} + \sum_{\substack{j=-\infty \\ j\neq 0}}^{\infty} \begin{pmatrix} p_{mn}^{(j)} \\ q_{mn}^{(j)} \end{pmatrix} \times \exp\left\{ i \left[-\vec{k}_s \cdot \vec{r}_{oj} + \frac{1}{2kr_0}((kr_{oj})^2 - (\vec{k}_s \cdot \vec{r}_{oj})^2) \right] \right\} \tag{4.7}$$

The phase of the incident plane wave can be expressed as:

$$\exp(i\vec{k}_i \cdot \vec{r}_0) = \exp(i\vec{k}_i \cdot \vec{r}_j) \exp(i\vec{k}_i \cdot \vec{r}_{0j}) \tag{4.8}$$

where $\vec{r}_{0j} = jh\hat{e}_z$, $j = \pm 1, \pm 2, \pm 3...$, h is the height of a sub-scatterer and $\vec{k}_i$ is the incident wave vector. In the situation of an infinite number of sub-scatterers, the relationship of scattering coefficients between the j-th and the 0-th sub-scatterers is:

$$\begin{pmatrix} p_{mn}^{(j)} \\ q_{mn}^{(j)} \end{pmatrix} = \exp(i\vec{k}_i \cdot \vec{r}_{0j}) \begin{pmatrix} p_{mn}^{(0)} \\ q_{mn}^{(0)} \end{pmatrix} \tag{4.9}$$

From Eq.(4.9), Eq.(4.7) can be simplified as:

$$\begin{pmatrix} p_{mn}^{o(0)} \\ q_{mn}^{o(0)} \end{pmatrix} = \begin{pmatrix} p_{mn}^{(0)} \\ q_{mn}^{(0)} \end{pmatrix} \sum_{j=-\infty}^{\infty} \exp\left\{ i \left[j(\vec{k}_i - \vec{k}_s) \cdot (h\hat{e}_z) + \frac{1}{2kr_0}((kr_{oj})^2 - (\vec{k}_s \cdot \vec{r}_{oj})^2) \right] \right\} \tag{4.10}$$

In the exponent, the second term is an infinitesimal quantity relative to the first

term. Subsequently, the scattering direction has the following restriction [19]:

$$(\vec{k}_s - \vec{k}_i) \cdot (h\hat{e}_z) = 2l\pi,\ l \in \{0, \pm 1, \pm 2, ...\} \tag{4.11}$$

The scattering and incident angles satisfy the following relationship:

$$\cos\theta_s = \cos\theta_i + \frac{2\pi l}{kh},\ l \in \{0, \pm 1, \pm 2, ...\}\ and\ |cos\theta_s| < 1 \tag{4.12}$$

where h must be the smallest periodic height and, θ_s and θ_i are the scattering and incident angles, respectively, relative to $\hat{e}_z$, which coincides with the direction of the scatterer with periodicity as shown in Figure 4.1. The smallest periodic length of a continuously 1-D periodic scatterer is 0. According to Eq.(4.12), l can only be 0, that is, $\theta_s = \theta_i$. Referring to the method of Draine and Flatau [19], the summation in Eq.(4.10) can be treated as an integration:

$$\begin{aligned}
&\sum_{j=-\infty}^{\infty} \exp\left\{ i \left[2jl\pi + \frac{1}{2kr_0}((kr_{0j})^2 - (\vec{k}_s \cdot \vec{r}_{oj})^2) \right] \right\} \\
&= \sum_{j=-\infty}^{\infty} \exp\left\{ i \left[j^2 \frac{(kh)^2 \sin^2\theta_s}{2kr_0} \right] \right\} \\
&\to \lim_{\epsilon \to 0^+} \int_{-\infty}^{\infty} dj \exp\left\{ i(1+i\epsilon) \left[j^2 \frac{(kh)^2 \sin^2\theta_s}{2kr_0} \right] \right\} \\
&= \frac{\sqrt{2\pi i k r_0}}{kh \sin\theta_s}
\end{aligned} \tag{4.13}$$

Similar to Eq.(4.5), the scattered field of a 1-D periodic scatterer can be represented as:

$$\mathbf{E}^{sca}(k\vec{r}_0)|_{kr_0 \to \infty} = \frac{exp(ikr_0)}{kr_0} \sum_{mn} \left[p_{mn}^{o(0)} \mathbf{A}_{mn}^{(p)}(\theta, \varphi) + q_{mn}^{o(0)} \mathbf{A}_{mn}^{(q)}(\theta, \varphi) \right] \tag{4.14}$$

In terms of Eqs.(4.10), (4.13), and (4.14), the scattered field is reduced from spherical to conical scattering:

$$\mathbf{E}^{sca}(k\vec{r}_0)|_{kr_0\to\infty} = \frac{\sqrt{2\pi i}}{kh\sin\theta_s}\frac{exp(ikr_0)}{\sqrt{kr_0}}\sum_{mn}\left[p_{mn}^{(0)}\mathbf{A}_{mn}^{(p)}(\theta,\varphi) + q_{mn}^{(0)}\mathbf{A}_{mn}^{(q)}(\theta,\varphi)\right] \quad (4.15)$$

Actually, the reduction is from the contribution of high order infinitesimal phase differences of the expansion coefficients for the scattered field in a different frame of reference because of an infinite number of sub-scatterers as described by Eqs.(4.5), (4.6), and (4.7). From Eq.(4.15), the scattered field of a 1-D periodic scatterer can be obtained if the scattering expansion coefficients $p_{mn}^{(0)}$ and $q_{mn}^{(0)}$ of the 0-th sub-scatterer are known.

Eq.(4.3) can be rearranged in terms of Eq.(4.9):

$$\begin{pmatrix} a_{mn}^{(0)} \\ b_{mn}^{(0)} \end{pmatrix} = \begin{pmatrix} a_{mn}^{o(0)} \\ b_{mn}^{o(0)} \end{pmatrix} + \sum_{n'=s}^{\infty}\begin{pmatrix} \bar{A}_{-mn'}^{-mn}(kh) & \bar{B}_{-mn'}^{-mn}(kh) \\ \bar{B}_{-mn'}^{-mn}(kh) & \bar{A}_{-mn'}^{-mn}(kh) \end{pmatrix}\begin{pmatrix} p_{mn'}^{(0)} \\ q_{mn'}^{(0)} \end{pmatrix} \quad (4.16)$$

where the series of equations have m-decoupled properties due to only axial translation and

$$\begin{pmatrix} \bar{A}_{-mn'}^{-mn}(kh) \\ \bar{B}_{-mn'}^{-mn}(kh) \end{pmatrix} = \sum_{\substack{j=-\infty \\ j\neq 0}}^{\infty}\begin{pmatrix} A_{-mn'}^{-mn}(k\vec{r}_{oj}) \\ B_{-mn'}^{-mn}(k\vec{r}_{oj}) \end{pmatrix}\exp(i\vec{k}_i\cdot\vec{r}_{oj}) \quad (4.17)$$

Eq.(4.17) can be approximately obtained through the truncation of infinite summation because of the convergence of A and B at infinity. Furthermore, incident and scattering expansion coefficients can be connected by the T-matrix:

$$\begin{pmatrix} p_{mn}^{(0)} \\ q_{mn}^{(0)} \end{pmatrix} = \sum_{m'n'} T_{mnm'n'}\begin{pmatrix} a_{m'n'}^{(0)} \\ b_{m'n'}^{(0)} \end{pmatrix} \quad (4.18)$$

Through Eqs.(4.16) and (4.18), we can obtain the matrix expression of the scattering expansion coefficients $p_{mn}^{(0)}$ and $q_{mn}^{(0)}$ of the 0-th sub-scatterer:

$$\begin{pmatrix} p^{(0)} \\ q^{(0)} \end{pmatrix} = \left(1 - T \begin{pmatrix} \bar{A} & \bar{B} \\ \bar{B} & \bar{A} \end{pmatrix} \right)^{-1} T \begin{pmatrix} a^{o(0)} \\ b^{o(0)} \end{pmatrix} \tag{4.19}$$

According to Eq.(4.19), the solution depends on the property of the T-matrix of a sub-scatterer. Consequently, if the sub-scatterer is axial rotationally symmetric, Eq.(4.19) will be m-decoupled; otherwise, only partially de-coupled or fully coupled. From Eqs.(4.15), (4.17), (4.18), and (4.19), the semi-analytical solution of a 1-D periodic solution can be obtained.

The scattering pattern of 1-D periodic scatterer is conical instead of spherical scattering in term of Eq.(4.15). Subsequently, in the consideration of the common definition of spherical scattering [22, 23] and the definition of infinite cylinder scattering [23], the amplitude scattering matrix is to be re-defined as:

$$\begin{pmatrix} E_{\theta\|\|}^{sca} \\ E_{\varphi|\perp}^{sca} \end{pmatrix} = \frac{\exp(ikr_0)}{\sqrt{kr_0}} \begin{pmatrix} s_{11} & s_{12} \\ s_{21} & s_{22} \end{pmatrix} \begin{pmatrix} E_{\theta\|\|}^{int} \\ E_{\varphi|\perp}^{int} \end{pmatrix} \tag{4.20}$$

where the subscripts θ and φ represent the components along zenithal and azimuthal directions and the subscript $\|$ and $\perp$ the parallel and perpendicular components relative to the scattering plane containing the incident and scattered directions. When the electric fields are expanded according to zenithal and azimuthal directions, it is called meridional plane expansion while scattering plane expansion is conducted with respect to the parallel and perpendicular directions relative to scattering plane. The definition of the Mueller matrix is the same as the one commonly employed [2, 22, 23].

Up to the present, the MBIT method has only been applied to scatterers with axial rotational symmetry [8, 9, 60]. For sub-scatterers without axial rotational symmetry, taking a hexagonal unit as an example, the method cannot be directly applied because the smallest circumscribed sphere of adjacent units will intersect with its side faces in addition to its vertices of end faces. In this case, we could treat the unit as an equivalent two-layer scatterer: the inner layer is the original unit and the outer layer, with the same refractive index as the surrounding medium, is its smallest circumscribed cylinder. According to a T-matrix formulation of multilayered scatterers [80], we can construct the same T-matrix relation as Eq.(4.18) between the incident and scattered field of the multilayered scatterer. After the treatment, the cylinder incident and scattering expansion coefficients are satisfied for use of the MBIT method [8, 9].

4.4 Validation of semi-analytical solution

The analytical solution of an infinite cylinder [22, 23] and the DDSCAT code [73, 19] are employed to validate the simulation results of continuous and discrete infinite scatterers calculated by the semi-analytical method. The scattering direction of a 1-D periodic scatterer is along either one or several particular angles according to Eq.(4.12). Subsequently, the scattering will only be restricted in azimuthal angles with certain zenithal angles. The incident and scattered field are expanded in the meridional plane in infinite cylinder comparisons, and are expanded in the scattering plane in discrete infinite cylinder comparisons. All incident and scattering angles are relative to laboratory frame of reference as shown in Figure 4.1, in which $\hat{e}_z$ coincides with the direction of a scatterer with periodicity.

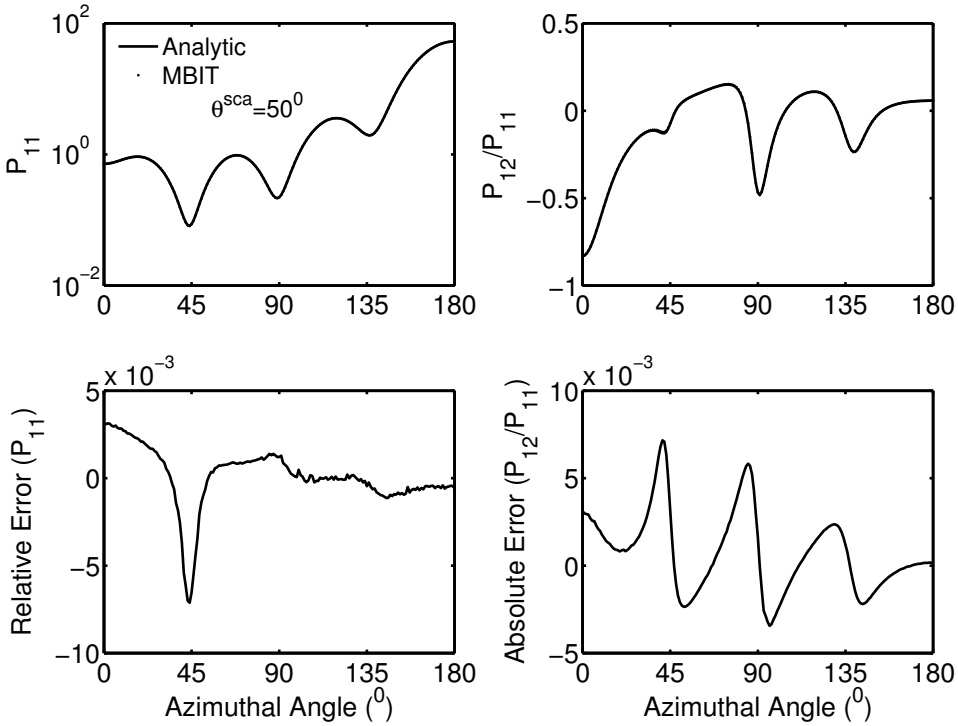

Figure 4.2: Comparisons of the Mueller matrix elements, P_{11} and P_{12}/P_{11} of infinite cylinder between analytical and the semi-analytical MBIT method calculated results.

Figure 4.2 shows the comparisons of the Mueller matrix elements, P_{11}(phase function) and P_{12}/P_{11}, of an infinite cylinder between analytical results and semi-analytical MBIT method calculated results. The cross-section diameter parameter is defined as $x_D = 2\pi D/\lambda = 10$ and the height parameter of a sub-scatterer as $x_H = 2\pi H/\lambda = 30$; the refractive index is $n = 1.33 + i0.01$; the incident angles are $\theta^{inc} = 50^0$, $\varphi^{inc} = 180^0$; and, the abscissas-axis represents the corresponding azimuthal angles. Due to scattering symmetry, only the results from 0^0 to 180^0 are displayed. The errors are displayed in the lower panels. In the vertical-axis labels, the relative error is defined as $(P_{11}(M) - P_{11}(A))/P_{11}(A)$ and the absolute error as

$P_{12}(M)/P_{11}(M) - P_{12}(A)/P_{11}(A)$, M is for MBIT, and A is for Analytic. The results agree well.

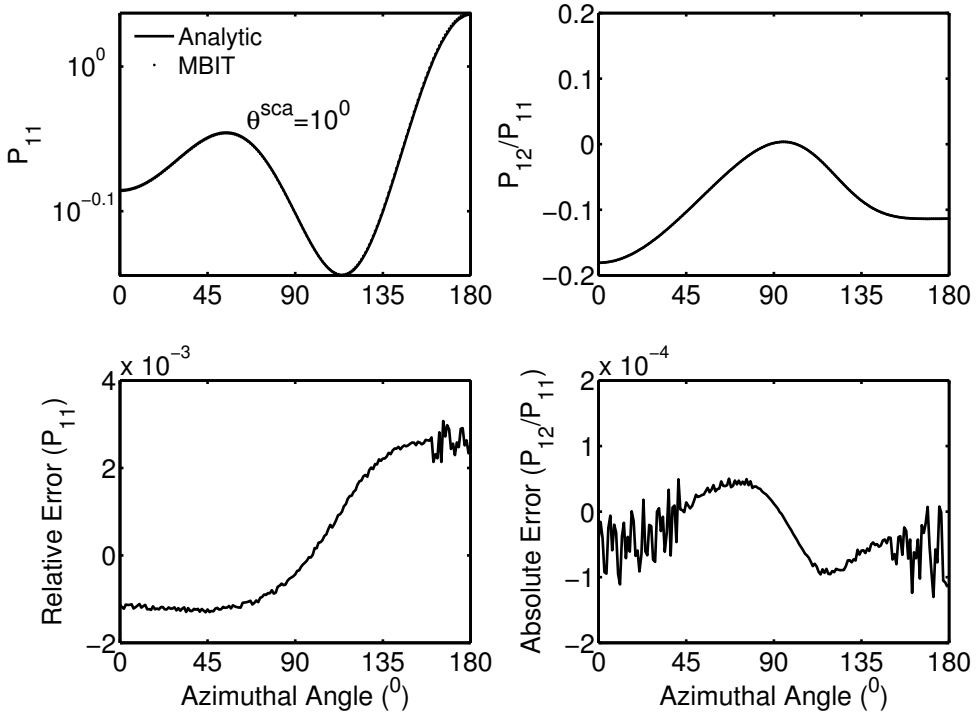

Figure 4.3: Comparisons of the Mueller matrix elements, P_{11} and P_{12}/P_{11} of an infinite cylinder between analytical results and the semi-analytical MBIT method calculated results.

Figure 4.3 shows the comparisons of the Mueller matrix elements, P_{11} and P_{12}/P_{11} of an infinite cylinder between analytical results and the semi-analytical MBIT method calculated results for a small incident angle. Incident angles are $\theta^{inc} = 10^0$, $\varphi^{inc} = 180^0$. The other parameters are the same as in Figure 4.2. Even at the small incident angle, the simulation results are in great agreement with the analytical

results.

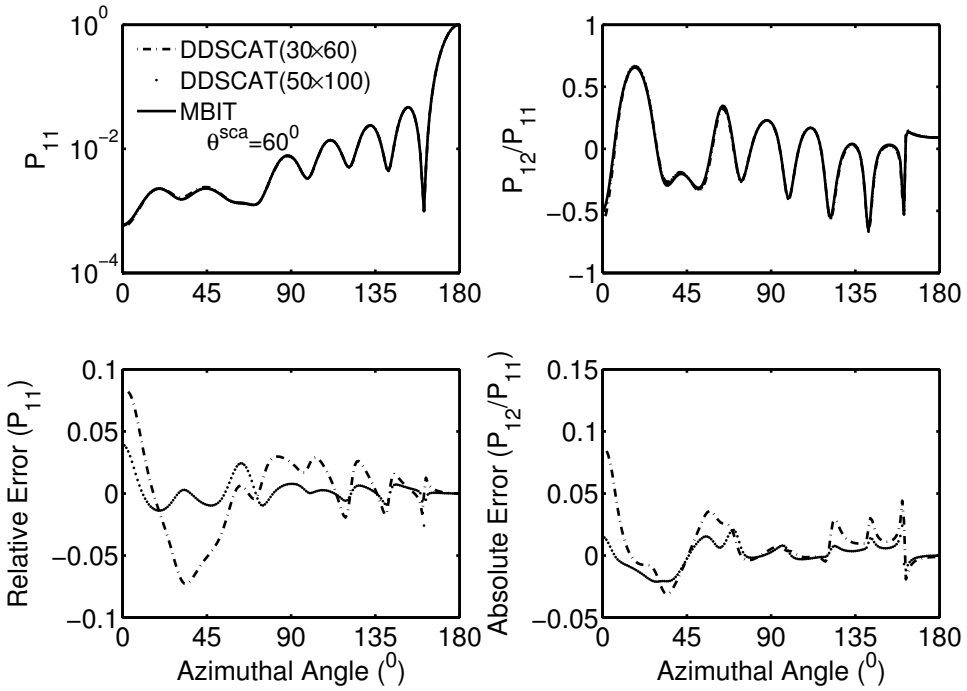

Figure 4.4: Comparisons of the Mueller matrix elements, P_{11} and P_{12}/P_{11} of an infinite discrete cylinder between the results calculated by DDSCAT and the semi-analytical MBIT method calculated results.

Figure 4.4 shows the comparisons of the Mueller matrix elements, P_{11} and P_{12}/P_{11} of an infinite discrete cylinder between the results calculated by DDSCAT and the semi-analytical MBIT method calculated results. The sub-scatterer is composed of a cylinder with $x_D = 20$ and $x_H = 10$ and a gap parameter $x_G = 2\pi G/\lambda$; G is the gap length; the refractive index is n=1.33+i0.01 ; and, the incident angles are $\theta^{inc} = 60^0, \varphi^{inc} = 180^0$. Only the results in the scattering cone $\theta^{sca} = 60^0$ are displayed. The DDSCAT results are displayed by two dipole numbers of 30 by 60

and 50 by 100 in the directions of height and diameter. As the dipole numbers increase, the numerically accurate method, DDSCAT, converges towards the results calculated by the semi-analytical method.

The above comparisons directly validate the semi-analytical solution for 1-D periodic scatterers. The following part will asymptotically compare scattering results from finite to infinite scatterers. The comparisons can indirectly validate the new method, but we also provide an intuitive concept of replacing the scattering properties of large aspect ratio finite-sized scatterers with the ones of infinite-sized scatterers.

4.5 Asymptotic comparisons from finite to infinite scatterers

The calculation time of the scattering properties of a finite scatterer is dependent on its size, shape, and refractive index while the one for the semi-analytical solution of a 1-D periodic scatterer only depends on the parameters of one sub-scatterer. Infinite scatterers are non-physical; however, large aspect ratio finite scatterers have scattering properties close to those of corresponding infinite scatterers. To a certain extent, infinite scatterers can replace the finite scatterers given that the calculation of the scattering properties of infinite scatterers are not too time-consuming to calculate relative to finite ones.

Figure 4.5 shows the asymptotic comparisons of the Mueller matrix elements, P_{11} and P_{12}/P_{11}, of cylinders between analytical and MBIT method calculated results. The cross-section diameter parameter is $x_D = 20$ for cylinders; the refractive index is $n = 1.33 + i0.01$; the incident angle is $\theta^{inc} = 60^0, \varphi^{inc} = 180^0$; and, N represents the aspect ratio of a finite cylinder, that is, x_H/x_D . The phase functions are normalized by the value at $\varphi^{sca} = 180^0$. The definitions of relative and absolute differences are the same as the ones of relative and absolute errors. From the difference comparisons,

we can conclude the phase function and P_{12}/P_{11} of finite cylinders with larger and larger aspect ratios are convergent toward the ones of the corresponding infinite cylinder. In this case, when the aspect ratio is equal to 12, the difference has an upper bound around ten percent.

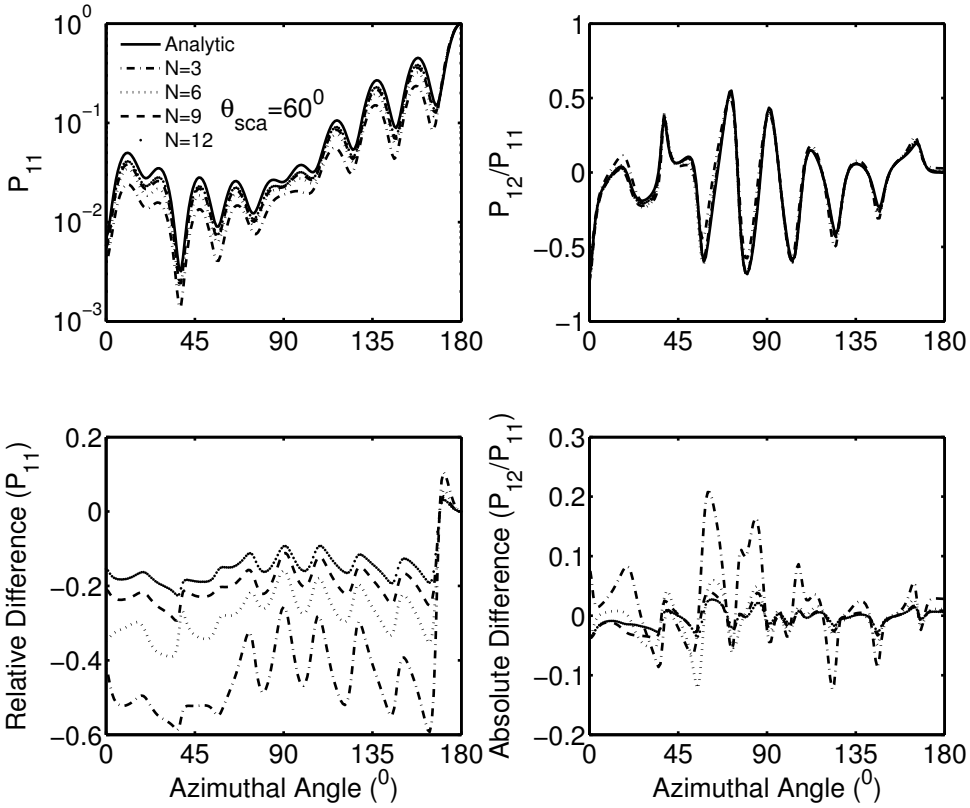

Figure 4.5: Asymptotic comparisons of the Mueller matrix elements, P_{11} and P_{12}/P_{11}, of cylinders between analytical results and the MBIT method calculated results.

Figure 4.6 shows the intuitive comparison of cylinders with increased aspect ratios. The parameters are the same as in Figure 4.5 except for $x_D = 10$ and $\varphi^{inc} = 0^0$.

The abscissa axis represents the azimuthal angles while the vertical axis the zenithal angles. The schematic phase function is on a logarithmic scale. With an increase in the aspect ratio, the scattering distribution is rapidly concentrated to certain scattering cones as expected from Eq.(4.12). In this figure, the scattering phase function does not have recognizable change when N goes from 12 to 21.

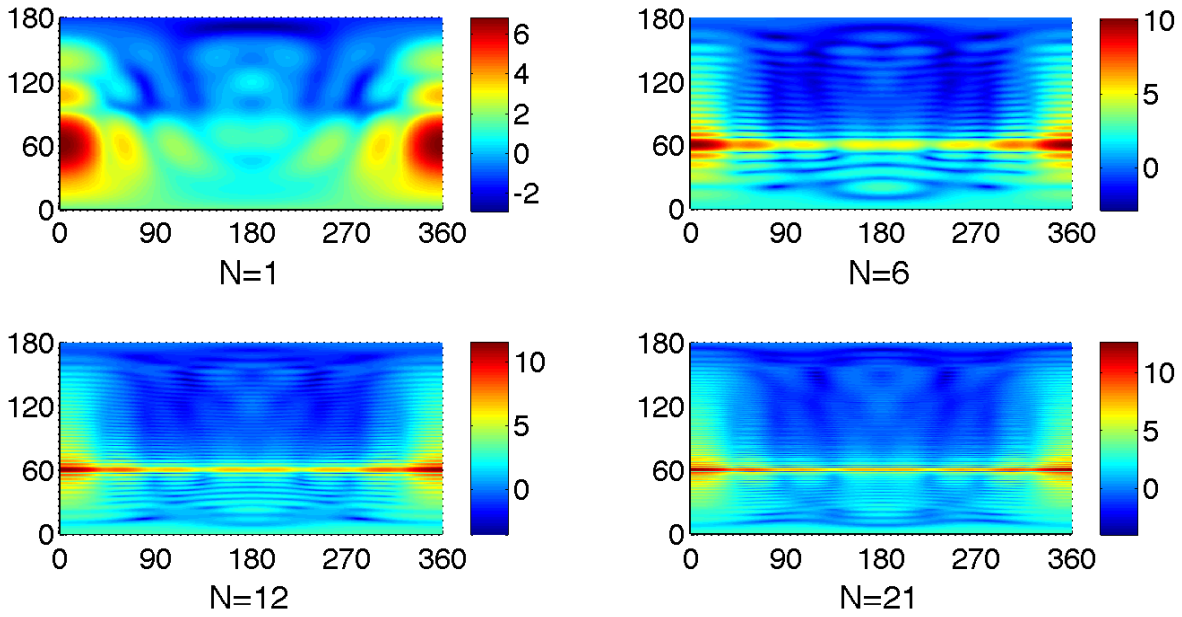

Figure 4.6: Asymptotic comparison of phase function of cylinders with different aspect ratios.

Figure 4.7 shows the phase function of discrete cylinders with 7 units. The unit is composed of a cylinder with $x_D = 10$, $x_H = 30$, and a gap with $x_G = 20$. Other parameters are the same as in Figure 4.6. The discrete cylinders display multiple scattering cones in large aspect ratios and the scattering angles are the ones expected from Eq.(4.12).

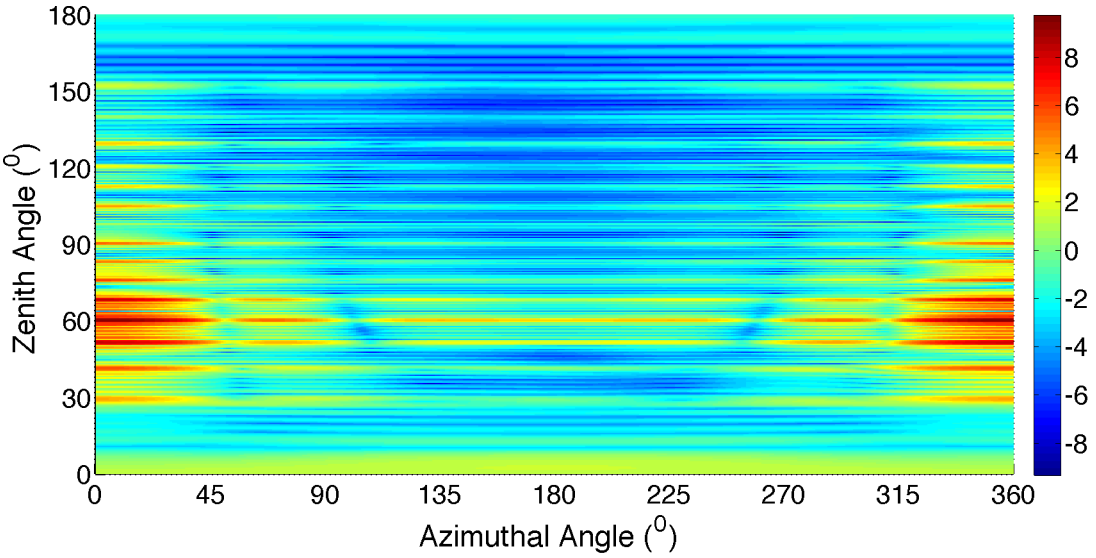

Figure 4.7: The phase function of discrete cylinders with 7 units.

Figure 4.8 shows the asymptotic comparisons of the Mueller matrix elements, P_{11} and P_{12}/P_{11}, of hexagonal scatterers with different aspect ratios. The diameter parameter of a cross-section circumscribed circle is $x_D = 10$; the refractive index is $n = 1.33 + i0.0$; the frame of reference origin is in the center of the hexagonal scatterer; the x-axis is perpendicular to one of the opposite sides as the left panel shows as shown in (c) of Figure 4.1; the incident angles are $\theta^{inc} = 60^0, \varphi^{inc} = 45^0$; and, N represents the aspect ratio of a hexagonal scatterer, that is, x_H/x_D . The T-matrix of a hexagonal prism is obtained by the II-TM method. Relative to the scatterer with a larger diameter of a cross section in Figure 4.5, the scattering pattern is rapidly convergent towards the pattern of scatterers with infinite aspect ratios.

Figure 4.9 shows that the asymptotic comparison of the phase function of hexagonal scatterers with different aspect ratios. As a continuation of Figure 4.8, the larger the aspect ratios, the more stable the scattering patterns.

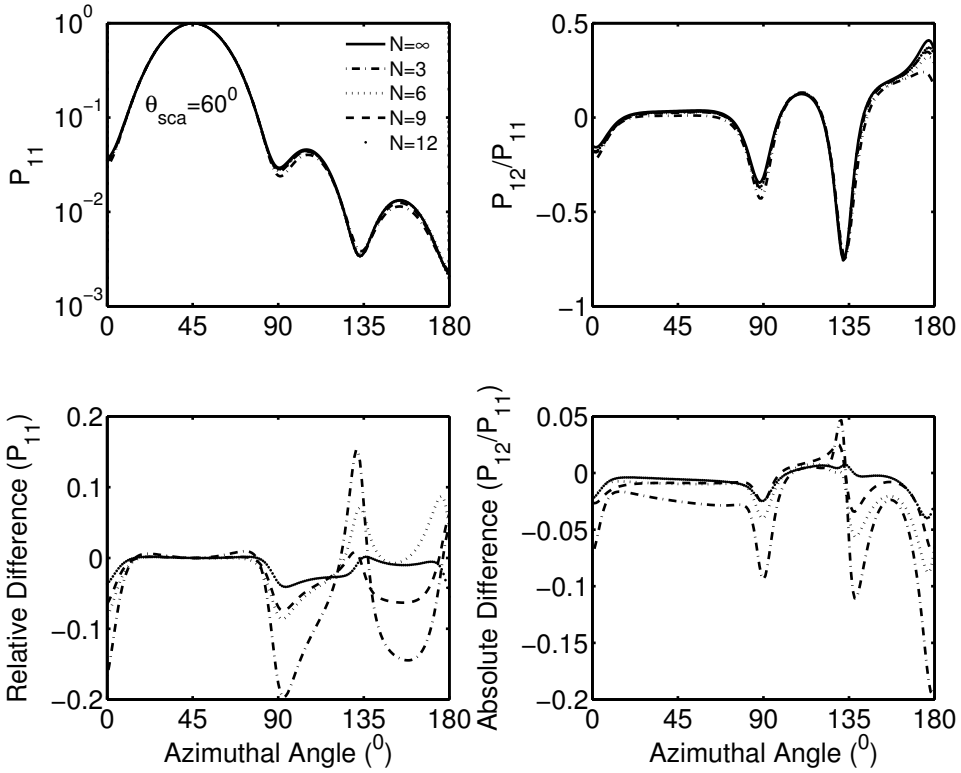

Figure 4.8: Asymptotic comparisons of the Mueller matrix elements, P_{11} and P_{12}/P_{11} of hexagonal scatterers with different aspect ratios.

4.6 Conclusion

Based on the MBIT method for finite scatterers with axially rotational symmetry, a semi-analytical solution of scattering properties is obtained for the infinite scatterers with 1-D periodic structures. The solution is validated by the analytic solution of an infinite cylinder and the DDA method with periodic boundary conditions. The preliminary comparisons of Mueller matrix elements between scatterers with different aspect ratios are displayed. The results illustrate that the scattering properties of large aspect ratio finite scatterers can be replaced by the scattering

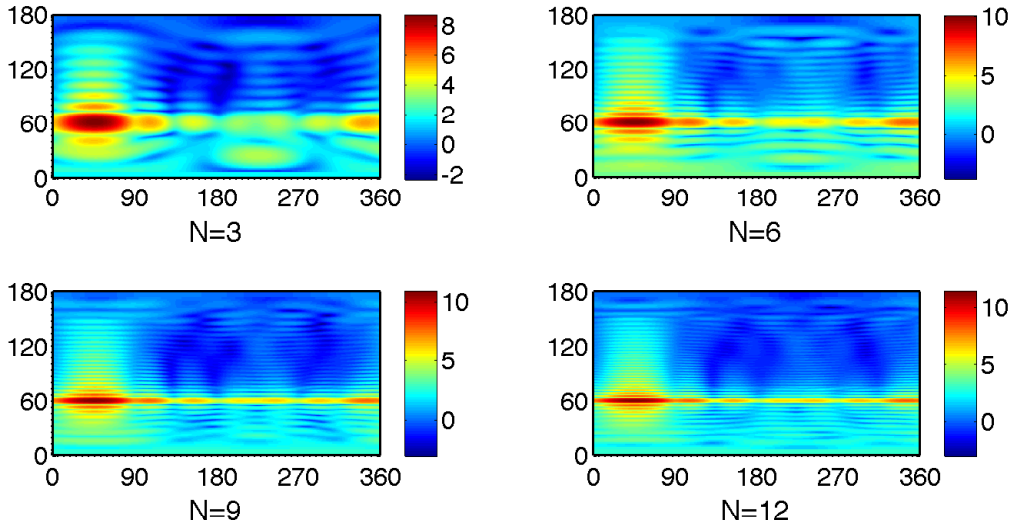

Figure 4.9: Asymptotic comparison of the phase function of a hexagonal scatterer with different aspect ratios.

properties of the corresponding infinite scatterers with 1-D periodic structures. The replacement depends upon the required accuracy. Since the II-TM can be applied to any shape to get its T-matrix, the semi-analytical solution can be effectively applied to any shape of a scatterer with 1-D periodic structures. However, the calculation efficiency of the T-matrix of a sub-scatterer is sensitive to its shape. Accordingly, the calculation efficiency and accuracy of the new method are sensitive to the shape of the sub-scatterer.

5. MARINE DIATOMS SCATTERING PROPERTIES IN TERMS OF MBIT METHOD

5.1 Introduction

In Section 1, Figure 1.2 shows the raw hologram of diatom chains within a phytoplankton thin layer in East Sound, WA, 2013 [21]. These chains are actually horizontally oriented with the action of current. The left panel of Figure 5.1 shows the diatom chain is formed by the connection of a series of individual cells. The right panel shows the shape of an individual cell, which has the siliceous outer hard shells with cytoplasm in its interior and connected spines. The material for the outer hard shells is essentially quartz glass so the refractive index relative to water is around 1.1 and the interior cytoplasm around 1.02. The relative refractive indices are close to unity, which means that the diatom chains in ocean are soft particles. Generally, the diffraction will dominate the forward scattering; however, the forward scattering for soft particles is dominated by the anomalous diffraction, which takes the interference between diffraction and direct transmission into considerations.

The scattering properties of an individual cell can be obtained in terms of invariant imbedding T-matrix method (II-TM), which is introduced in Section 2. The MBIT method introduced in Section 3 and Section 4 can be properly applied on diatom chains to obtain their scattering properties. For facet or simple scatterers (e.g. right cylinders), the diffraction and anomalous diffraction can be obtained analytically.

The scattering properties of a single chain is the foundation for the scattering of oceanic scatterers. For instance, the bulk scattering properties can be obtained after considering certain particle size distributions. In this study, we are focusing

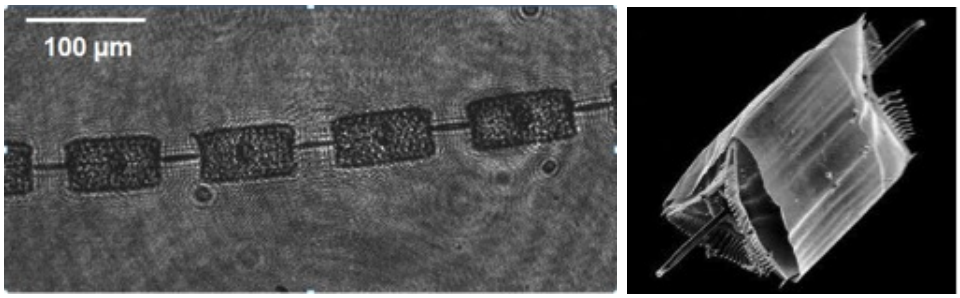

Figure 5.1: A diatom chain and the shape of an individual unit (From Nagumo et al. [81]).

on the effect on scattering properties exerted by a single diatom chain with different compositions, shapes, and orientations. In 5.2, the simulation model and methods are introduced. The simulation results are presented in 5.3. Conclusion will be given in 5.4.

5.2 Simulation model and methods

5.2.1 Simulation model

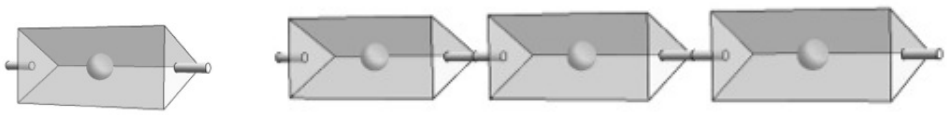

Figure 5.2: Simulation model for an individual cell and diatoms chains. The right panel shows three units aligned in the main axis direction.

The right panel of Figure 5.1 roughly shows a trigonal prism with a core and two connected spines. Consequently, the simulated model is taken as a prism based on an equilateral trigon with a spherical core in the center of the prism and two spines

connected to the centers of the two bottoms of the prism, which is shown in the left panel of Figure 5.2. The diatom chain is constructed by stacking the units along the direction of the main axis. The right panel of Figure 5.2 shows a chain with 3 units.

The particle frame of reference has to be set since the T-matrix is dependent on the orientation of a scatterer. The main axis of an individual cell is set to be the z-axis of the particle frame of reference and the x-axis is pointing to one of the vertices in the plane perpendicular to the main axis, which are shown in Figure 5.3. The origin is always in the center of a scatterer. For diatom chains, the same configuration is still employed. An individual cell or diatom chain has σ_h, σ_{xz}, C_3 symmetries and a C_2 symmetry perpendicular to the main axis according to Section 2. The calculation efficiency has been dramatically increased after taking all these symmetries into consideration.

5.2.2 Simulation methods

According to the configurations of the diatom chains, the MBIT method, which was introduced in detail in Section 3, is a great option to obtain their scattering properties.

For particles with $|m-1| \ll 1$ and $x = 2\pi L/\lambda$, m is the refractive index of a scatterer and L is the characteristic length and λ the incident wavelength, the anomalous diffraction theory (ADT) [22] can be invoked to compare the simulation results of forward directions with accurate results. The ADT approximates the field in the region beyond the scatterer and keeps the same the amplitude like the absence of a scatterer, but the phase is changed.

The electric field in the far field region can be formulated as the surface integral

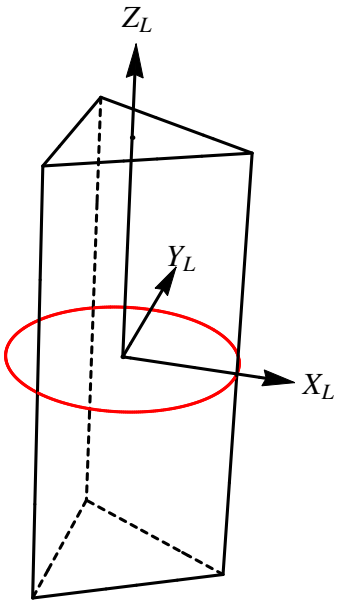

Figure 5.3: Particle frame of reference of an individual unit.

of electromagnetic field [40, 49]:

$$\mathbf{E}^{sca}(\vec{r})|_{kr\to\infty} = \frac{\exp(ikr)}{-ikr}\frac{k^2}{4\pi}$$
$$\hat{e}^{sca} \times \oint_s \{\hat{n}_s \times \mathbf{E}(\vec{r}') - \hat{e}^{sca} \times [\hat{n}_s \times \mathbf{H}(\vec{r}')]\} \exp(-ik\hat{e}^{sca} \cdot \vec{r}') d^2\vec{r}' \qquad (5.1)$$

where $\hat{e}^{sac}$ represents scattering direction, s is the scatterer surface and $\hat{n}_s$ is the outward unit vector normal to the surface s.

Eq.(5.1) is also called Kirchhoff surface integral, which is mapping the near field to far field. Accordingly, the contribution of Kirchhoff diffraction can be obtained by mapping the incident field of the illuminated sides to far field. The diffractions obtained by this surface integral is normally different from the one obtained by Babi-

net's principle except for the exact forward direction [22, 82]. For soft particles, the contribution of direct transmission has to be considered since the direct transmission has a strong destructive interference with diffraction, which can be obtained by mapping the electromagnetic field of un-illuminated sides to far field. The direct reflection contribution has been ignored according to ADT. Consequently, the anomalous diffraction consists of diffraction and direct transmission.

For facet particles, the diffraction and anomalous diffraction can be obtained analytically [50, 52, 82]:

$$\mathbf{S} = \sum_{j=1}^{N} D_j \bar{\mathbf{S}}^{(j)} \tag{5.2}$$

$$D_j = \frac{k^2}{4\pi} \exp[ik(\hat{e}^{inc} - \hat{e}^{sca}) \cdot \vec{r}_{j,1}] C_j \int_{s_j} \exp[ik(\vec{A}_j - \hat{e}^{sca}) \cdot \vec{\omega}_j d^2\vec{\omega}_j] \tag{5.3}$$

$$\bar{S}_{11}^{(j)} = \sin\theta(\hat{n}_{s_j} \cdot \hat{e}_{\parallel}^{sca}) - \cos\theta[(\vec{A}_j + \hat{e}^{sca}) \cdot \hat{n}_{s_j}] + (\hat{n}_{s_j} \cdot \hat{e}_{\parallel}^{inc})(\vec{A}_j \cdot \hat{e}_{\parallel}^{sca}) \tag{5.4}$$

$$\bar{S}_{12}^{(j)} = (\hat{n}_{s_j} \cdot \hat{e}_{\perp})(\vec{A}_j \cdot \hat{e}_{\parallel}^{sca}) \tag{5.5}$$

$$\bar{S}_{21}^{(j)} = \sin\theta(\hat{n}_{s_j} \cdot \hat{e}_{\perp}) + (\hat{n}_{s_j} \cdot \hat{e}_{\parallel}^{inc})(\vec{A}_j \cdot \hat{e}_{\perp}) \tag{5.6}$$

$$\bar{S}_{22}^{(j)} = -(\vec{A}_j + \hat{e}^{sca}) \cdot \hat{n}_{s_j} + (\hat{n}_{s_j} \cdot \hat{e}_{\perp})(\vec{A}_j \cdot \hat{e}_{\perp}) \tag{5.7}$$

where the incident wave is $\mathbf{E}_0 \exp(ik\hat{e}^{inc} \cdot \vec{r})$, j enumerates the faceted surfaces, θ is the scattering zenith angle, $\hat{e}_{\parallel}^{sac,inc}$ and $\hat{e}_{\perp}$ are related to the scattering plane, $\vec{r}_{j,1}$ is the position vector of the first vertex of the j-th surface, ω_j is the position vector in surface s_j, and C_j and $\vec{A}_j$ are defined as:

$$C_j = \begin{cases} 1 & \text{for Diffraction} \\ \exp[i(m-1)k\delta r_{j,1}] & \text{for Direction transmission of ADT} \end{cases} \tag{5.8}$$

$$\vec{A}_j = \begin{cases} \hat{e}^{inc} & \text{for Diffraction} \\ (m-1)\frac{\hat{n}_l}{\hat{e}^{inc} \cdot \hat{n}_l} + \hat{e}^{inc} & \text{for Direction transmission of ADT} \end{cases} \tag{5.9}$$

where m is the refractive index of a soft scatterer, $(m-1)\delta r_{j,1}$ is the optical path length difference of the first vertex of the j-th surface compared to the absence of the scatterer, which is related to the outward normal vector to the last faceted surface [52], and $\hat{n}_l$ is the outward unit vector normal to the last surface before hitting the current surface. The integral in Eq.(5.3) can be analytically obtained [83, 82]:

$$\frac{k^2}{4\pi}\int_s \exp[ik\vec{B}\cdot\omega_j]d^2\omega_j = \frac{ik}{4\pi}\sum_{k=1}^{N_v}\{\frac{(\vec{\omega}_{k+1}-\vec{\omega}_k)\cdot(\vec{B}\times\hat{n}_s)}{|B|^2-(\vec{B}\cdot\hat{n}_s)^2}\}$$
$$\{\frac{\sin k[\vec{B}\cdot(\vec{\omega}_{k+1}-\vec{\omega}_k)/2]}{k[\vec{B}\cdot(\vec{\omega}_{k+1}-\vec{\omega}_k)/2]}\}\exp[ik\vec{B}\cdot(\vec{\omega}_{k+1}+\vec{\omega}_k)/2] \tag{5.10}$$

where $\vec{B}$ is not related to the current surface s, $\vec{\omega}$ is the position vector in surface s, the order of the vertices is along the outward unit vector $\hat{n}_s$, N_v is the number of vertices in surface s and $\vec{\omega}_{N_v+1} = \vec{\omega}_1$. For the cylinder, if the incident direction is perpendicular to the rotational axis, the diffraction and anomalous diffraction can also be easily obtained.

5.3 Simulation results

In this part, diatom chains will be studied to see the effects on scattering properties created by different compositions, shapes and orientations. For the following simulation results, the parameters for an individual cell are employed: the height of a trigonal prism is 40 (hereafter the length is normalized by $\lambda/2\pi$), the diameter of the circumscribed circle of the bottom trigon is 20, the diameter of the spherical core inside the prism is 2 and the length and bottom diameter of a single cylindrical spine are 7.5 and 2; the refractive index for the spherical shell is 1.02+i0.0 and other parts 1.1+i0.0, respectively. All of the incident angles are denoted relative to the laboratory frame of reference and all the scattering results are shown relative to the incident frame reference. Figure 5.4 shows the incident and laboratory frame of ref-

erences. The left panel shows the position of incident frame of reference (denoted as subscript I) in the laboratory frame of reference (denoted as subscript L) in terms of the incident angles θ_I and ϕ_I . The scattering results of certain scattering direction $\hat{e}^{sac}$ are shown relative to the incident frame of reference, which is shown in the right panel.

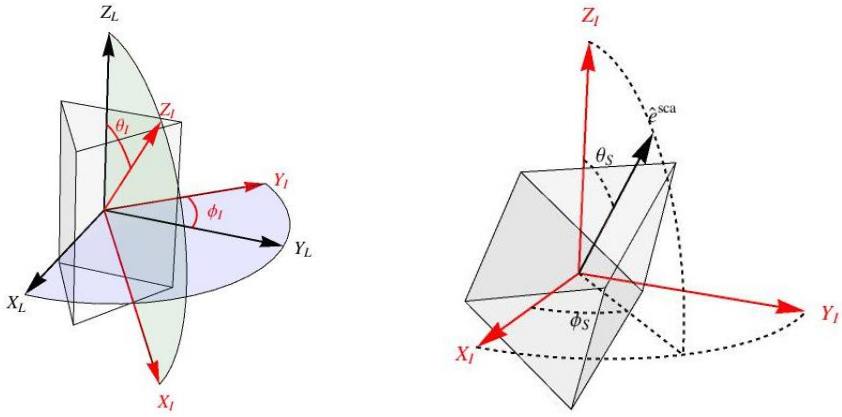

Figure 5.4: Incident and laboratory frames of references. The left panel shows the position of incident frame of reference (denoted as subscript I) in the laboratory frame of reference (denoted as subscript L) in terms of the incident angles θ_I and ϕ_I . The scattering results of certain scattering direction $\hat{e}^{sac}$ are shown relative to the incident frame of reference, which is shown in the right panel.

Figure 5.5 shows the comparisons of the Mueller matrix elements of a single diatom when it has different compositions: with a spherical core only, two spines only, or both, or none of them, which are denoted in the legends according to the meaning. The incident angle relative to the laboratory frame of reference is $(60^0, 0^0)$ and the abscissa axis from 0^0 to 180^0 is the scattering angle relative to the incident frame of reference. The appreciable discrepancy in the backward scattering can be

observed from elements p_{11} and p_{22}/p_{11} for different compositions. The presence of the spines has brought more effect on backward scattering than the presence of the core.

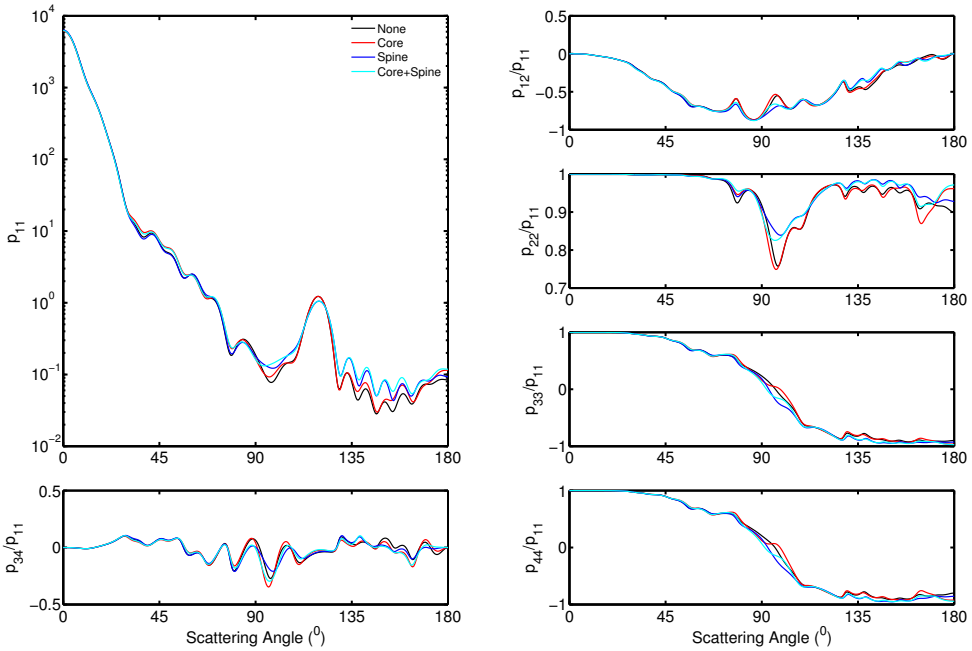

Figure 5.5: Comparisons of the Mueller matrix elements of a single diatom when it has a core ('Core'), two spines ('Spine'), a core and two spines ('Core+Spine'), or none of them ('None'), respectively.

Figure 5.6 shows the backward scattering of the Mueller matrix elements, P_{11} and P_{12}/P_{11}, of a single diatom when it has a core ('Core'), two spines ('Spine'), a core and two spines ('Both'), or none of them ('None'), respectively. The figure is centered with zenith angle 180^0 and bounded by zenith angle 90^0, and the angles between 90^0 and 180^0 are equally divided according to the radius [84]. The discernible differences

can be observed through the elements. The effect caused by the presence of the core and spines cannot be ignored.

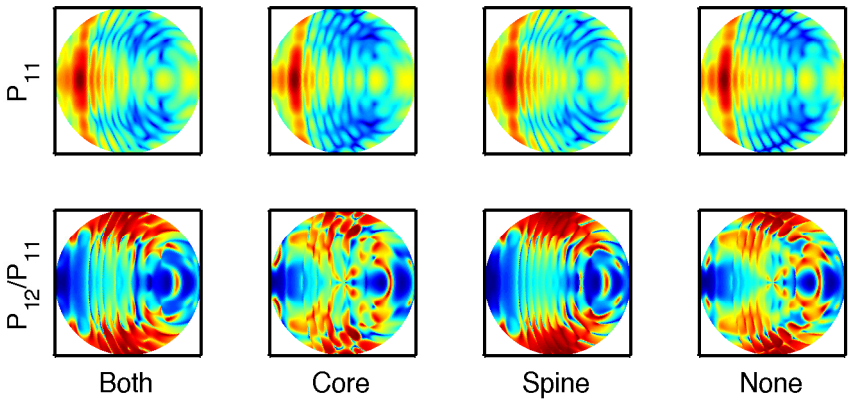

Figure 5.6: Backward scattering of the Mueller matrix elements, $P_{11}$and P_{12}/P_{11}, of a single diatom when it has a core ('Core'), two spines ('Spine'), a core and two spines ('Both'), or none of them ('None'), respectively.

Figure 5.7 shows the comparisons of the Mueller matrix elements of a diatom chain with one unit, two units, four units and fifteen units. The configuration is the same as Figure 5.5. The interaction is becoming stronger and stronger with the increased number of units. The elements, p_{12}/p_{11}, p_{33}/p_{11}, and p_{44}/p_{11}, display a similar pattern with Rayleigh-Gan's scattering for one, two, or four units [22, 23] whereas these elements show a strong interference pattern for fifteen units.

Figure 5.8 shows the comparisons of the Mueller matrix elements a diatom chain with fifteen units in fixed and random orientations. The configuration for the fixed orientation results is the same as Figure 5.5. The scattering patterns of all elements are smoothed out by the average of random orientations. The orientation information

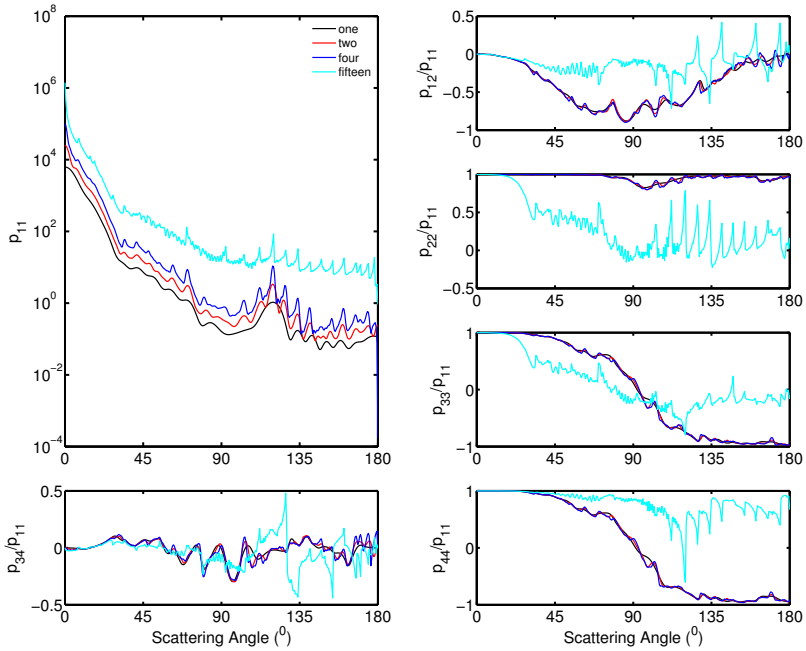

Figure 5.7: Comparisons of the Mueller matrix elements of a diatom chain with one unit, two units, four units, and fifteen units. The configuration is the same as Figure 5.5.

can be detected in terms of the scattering patterns.

Figure 5.9 shows the Mueller matrix elements of a diatom chain with 15 units with the incident normal to the main axis and comparisons of the phase function in forward scattering between diffraction, anomalous diffraction and the MBIT method. In ocean, the diatom chains are actually horizontally aligned by the action of current. The sunlight will roughly illuminate the diatoms in the direction perpendicular to the main axis. The incident zenith angle is set to be 90^0. The shape has 3-fold rotational symmetry instead of axial rotational symmetry. The different incident azimuthal angles will produce different scattering patterns. Consequently, the result

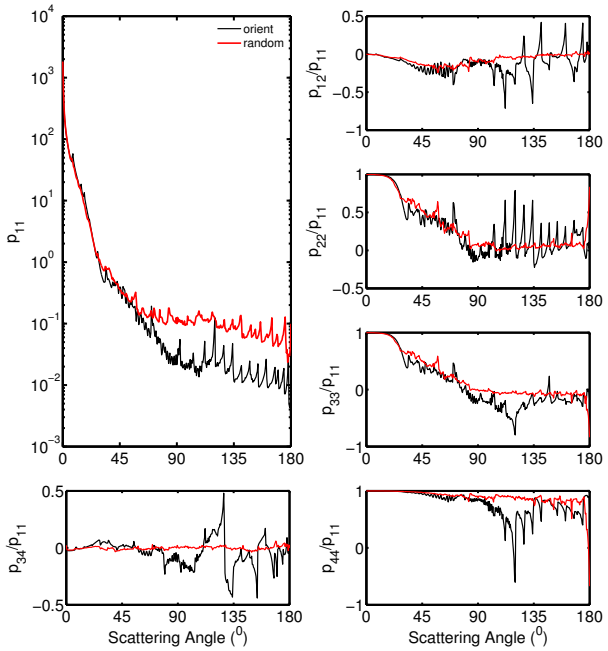

Figure 5.8: Comparisons of the Mueller matrix elements a diatom chain with fifteen units in fixed and random orientations. The configuration for the fixed orientation results is the same as Figure 5.5.

is averaged with the azimuthal angles for a fixed zenith angle. In this orientation, the elements, p_{12}/p_{11}, p_{33}/p_{11}, and p_{44}/p_{11}, show a pattern similar to Rayleigh-Gan's scattering. The reason for that is the units in the chains for this normal incidence have small interactions.

The inset in the p_{11} panel shows a large discrepancy in the forward scattering between diffraction and the numerically accurate solution MBIT whereas the anomalous diffraction theory displays a better agreement. For soft particles, the forward direction is dominated by the anomalous diffraction instead of the general diffraction. For the light scattering of red blood cells, the similar conclusion has been

drawn [85]. When the refractive index is approaching unity, the direct transmitted light will have small deviations associated with the incident direction and will have stronger and stronger destructive interference with the general diffraction. In the limit, the diffraction and the direct transmission would be completely destructive, which makes the scattering disappear, if the refractive index is unity. Therefore, the interference between diffraction and direct transmission for the soft particles has to be taken into considered in conventional geometric optics methods.

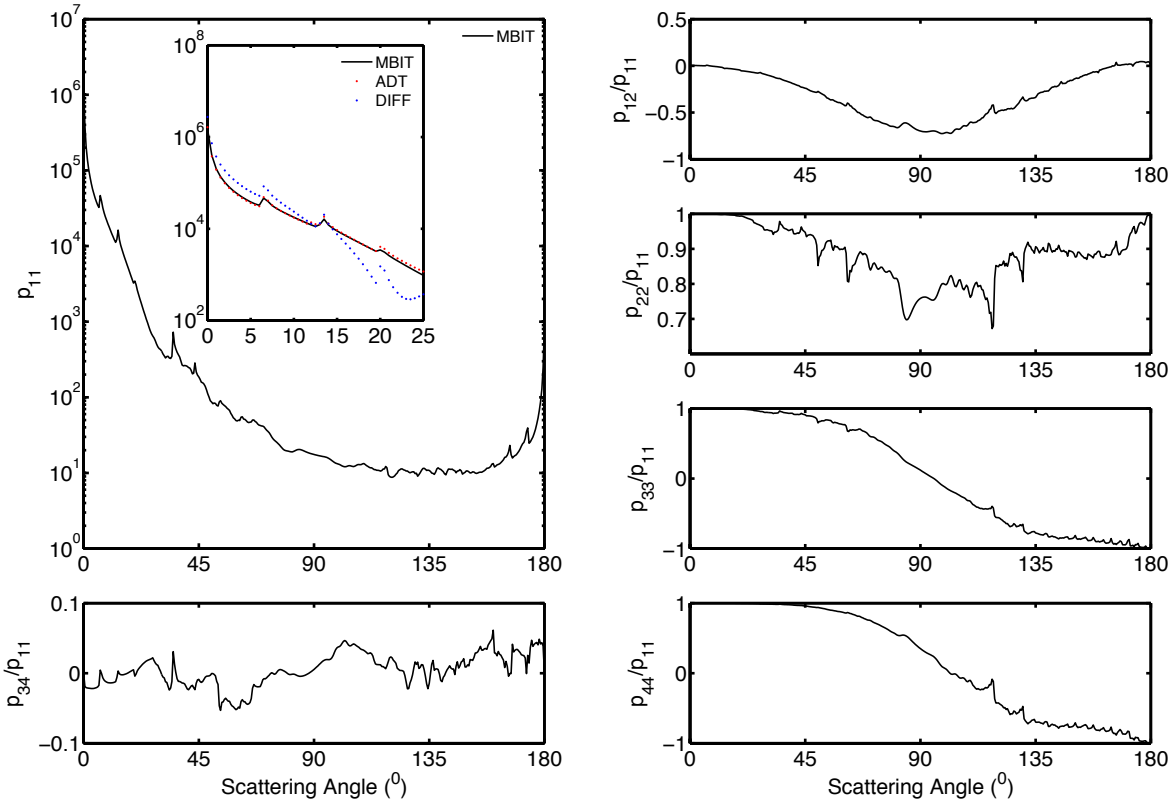

Figure 5.9: Mueller matrix elements of a diatom chain with 15 units with the incident normal to the main axis and Comparisons of the phase function in forward scattering between diffraction, anomalous diffraction and the MBIT method.

Figure 5.10 shows the comparisons of the Mueller matrix elements of the prisms based on different orders of equilateral polygons. For instance, prism3 represents the prism based on an equilateral trigon and prism∞ represents actually a cylinder with the same height as the prisms and the same diameter as the circumscribed circle of the bottom polygons of the prisms. The diameter of the circumscribed circle of bottom polygons of the prisms is taken to be 20 and the height of the prisms 20. The prisms are set to be homogeneous and the refractive index is 1.1+i0.0. The incident polar angle is 60^0 and the azimuthal angle is $180^0/N$, where N is the order of bottom polygon. The incident light is always on the vertical edge of the prisms. With the increased order of bottom polygons, the scattering patterns are approaching the scattering results of the corresponding cylinder. The element p_{22}/p_{11} is much more sensitive to the order than other elements. The element p_{22}/p_{11} is also the indicator of non-sphericity [23]. It can be the element to detect the shape information.

5.4 Conclusion

In this section, the MBIT method is applied to get the scattering properties of diatom chains. The individual cell has some interior structures and spines connecting on it. The effects of the structures are simulated in terms of invariant imbedding T-matrix method. For diatoms in the ocean, they have some specific orientations due to the action of current. The sunlight will incident on the diatoms perpendicular to the main axis. The scattering patterns are shown for the different orientations and random orientation. The orientation information can be detected in terms of the scattering properties. The diatom is modeled as a prism based on an equilateral trigon. The scattering results of prisms with different order of bottom polygons are shown. The element p_{12}/p_{11} is more sensitive to the order than other elements, which can be used as the indicator of shape detection.

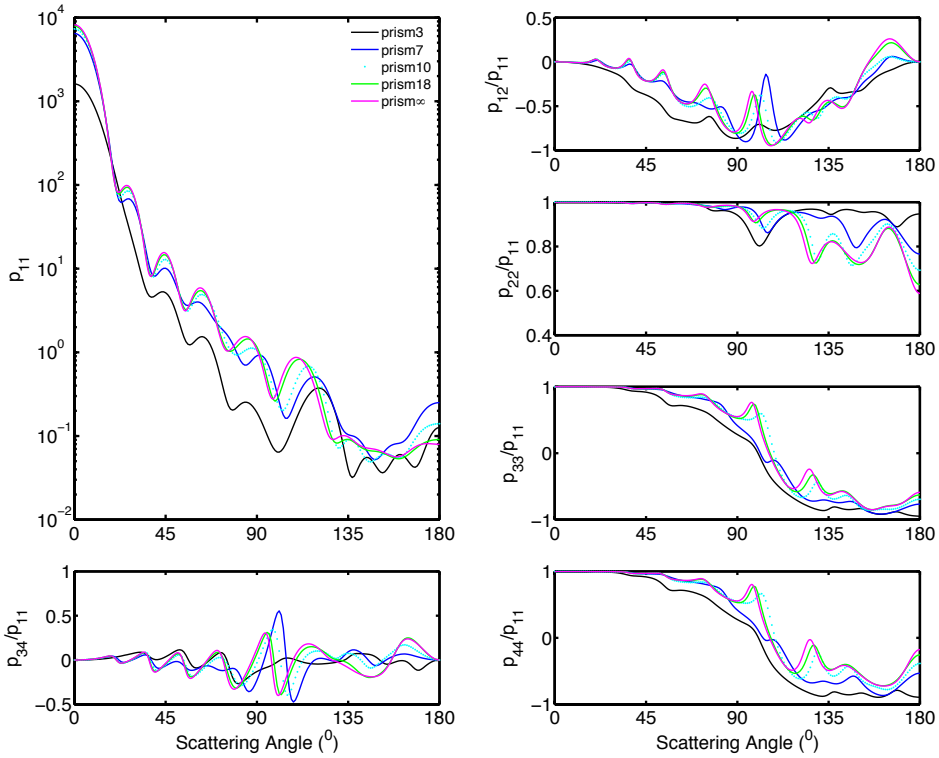

Figure 5.10: Comparisons of the Mueller matrix elements of prisms based on different orders of equilateral polygons. For instance, prism3 represents the prism based on an equilateral trigon. prism∞ represents actually a cylinder with the same height as the prisms and the same diameter as the circumscribed circle of the bottom polygons of the prisms.

The relative refractive index of scatterers in the ocean is close to unity, which are so-called soft particles. The forward scattering for soft particles is dominated by the anomalous diffraction, which contains the interference between the diffraction and direct transmission, instead of diffraction. In this case, the diffraction and anomalous diffraction can be obtained analytically. The comparisons confirm the dominant contribution of anomalous diffraction.

6. CONCLUSION

Extended boundary condition method (EBCM) and Invariant Imbedding T-matrix (II-TM) method are two of the most efficient techniques for the realization of T-matrix method, especially for scatterers with axial or N-fold rotational symmetries. The calculation efficiency is highly dependent on the size parameter, refractive index, shape and aspect ratio of a scatterer. Of these factors, the aspect ratio plays an important role. With the increased aspect ratios of a scatterer, the EBCM will encounter ill-conditioned problems and the II-TM will have much more memory requirements and time consumption. Based on the transition matrix of a scatterer, a method called many-body iterative T-matrix is developed to target scatterers with large aspect ratios. The original scatterer is divided into several sub-scatterers. The scattering of the original scatterer can be iteratively obtained in terms of the transition matrices of the sub-scatterers. In this case, the many-body scattering condition that the circumscribed spheres of scattering particles cannot intersect is avoided by using the boundary conditions on the adjacent sub-scatterers.

For scatterers with large aspect ratios, the scattering of the counterpart with one dimension periodicity would be a good proxy. Based on the MBIT method, a semi-analytical solution for a scatterer with 1-D periodicity is obtained in terms of direct matrix inverse instead of iteration. The method is verified by the comparisons between simulations results and, the analytical solution of an infinite cylinder and the numerically accurate method (DDA), and by the scattering tendency of scatterers with larger and larger aspect ratios. Some of the marine scatterers, such as diatoms, have a specific chain structure, which are formed by the connection of many individual cells and also have preferential orientations due to current flow. More-

over, the relative refractive indices of the scatterers are close to unity, which are so-called soft particles. The diatom chains are simulated using the MBIT method to obtain the effects on scattering properties for different compositions, shapes and orientations. Forward scattering for soft particles is dominated by the anomalous diffraction, which includes the interference between diffraction and direct transmission, instead of general diffraction. The conclusion is confirmed by the comparisons between the analytical calculation of the diatoms for the diffraction and anomalous diffraction, and the numerically simulation using the MBIT method.

REFERENCES

[1] L. Tsang, J. A. Kong, and K. H. Ding. *Scattering of Electromagnetic Waves, Theories and Applications*, volume 27. John Wiley & Sons, New York, 2004.

[2] M. I. Mishchenko, L. D. Travis, and A. A. Lacis. *Scattering, Absorption, and Emission of Light by Small Particles*. Cambridge University Press, Cambridge, 2002.

[3] F. M. Schulz, K. Stamnes, and J. J. Stamnes. Point-group symmetries in electromagnetic scattering. *J. Opt. Soc. Am. A*, 16(4):853–865, 1999.

[4] P. C. Waterman. Matrix formulation of electromagnetic scattering. *Proc. IEEE*, 53(8):805–812, 1965.

[5] P. C. Waterman. Symmetry, unitarity, and geometry in electromagnetic scattering. *Phys. Rev. D*, 3(4):825, 1971.

[6] B. R. Johnson. Invariant imbedding T-matrix approach to electromagnetic scattering. *Appl. Opt.*, 27(23):4861–4873, 1988.

[7] L. Bi, P. Yang, G. W. Kattawar, and M. I. Mishchenko. Efficient implementation of the invariant imbedding T-matrix method and the separation of variables method applied to large nonspherical inhomogeneous particles. *J. Quant. Spectrosc. Radiat. Transfer*, 116:169–183, 2013.

[8] W. Yan, Y. Du, H. Wu, D. Liu, and B. Wu. EM scattering from a long dielectric circular cylinder. *Prog. Electromagn. Res.*, 85:39–67, 2008.

[9] B. Sun, P. Yang, and G. W. Kattawar. Many-body iterative T-matrix method for large aspect ratio particles. *J. Quant. Spectrosc. Radiat. Transfer*, 127:165–175, 2013.

[10] D. R. Fokkema. Enhanced implementation of bicgstab (l) for solving linear systems of equations. *Preprint*, 976, Universiteit Utrecht, Department of Mathematics, 1996.

[11] P. C. Chaumet and A. Rahmani. Efficient iterative solution of the discrete dipole approximation for magnetodielectric scatterers. *Opt. Lett.*, 34(7):917–919, 2009.

[12] J. Tang, Y. Shen, Y. Zheng, and D. Qiu. An efficient and flexible computational model for solving the mild slope equation. *Coastal Eng.*, 51(2):143–154, 2004.

[13] J. H. Bruning and Y. Lo. Multiple scattering of EM waves by spheres Part I–multipole expansion and ray-optical solutions. *IEEE Trans. Antennas Propag.*, 19(3):378–390, 1971.

[14] D. W. Mackowski. Analysis of radiative scattering for multiple sphere configurations. *Proc. R. Soc. London, Ser. A*, 433(1889):599–614, 1991.

[15] W. C. Chew. Recurrence relations for three-dimensional scalar addition theorem. *J. Electromagnet. Wave*, 6(1-4):133–142, 1992.

[16] Y. Xu. Calculation of the addition coefficients in electromagnetic multisphere-scattering theory. *J. Comput. Phys.*, 127(2):285–298, 1996.

[17] V. P. Walden, S. G. Warren, and E. Tuttle. Atmospheric ice crystals over the antarctic plateau in winter. *J. Appl. Meteorol.*, 42(10):1391–1405, 2003.

[18] B. Sun, P. Yang, G. W. Kattawar, and L. Bi. Scattering of 1-D periodic scatterer and asymptotic comparison using the many-body iterative T-matrix method. *J. Quant. Spectrosc. Radiat. Transfer*, 2014.

[19] B. T. Draine and P. J. Flatau. Discrete-dipole approximation for periodic targets: theory and tests. *J. Opt. Soc. Am. A*, 25(11):2693–2703, 2008.

[20] A. F. Oskooi, D. Roundy, M. Ibanescu, P. Bermel, J. D. Joannopoulos, and S. G. Johnson. MEEP: A flexible free-software package for electromagnetic simulations by the fdtd method. *Comput. Phys. Commun.*, 181(3):687–702, 2010.

[21] J. M. Sullivan. A submersible holographic camera for the undisturbed characterization of optically relevant particles in water (holocam). Technical report, WET LABS INC NARRAGANSETT RI RESEARCH DEPT., 2011.

[22] H. C. Van De Hulst. *Light Scattering by Small Particles*. John Wiley & Sons, New York, 1981.

[23] C. F. Bohren and D. R. Huffman. *Absorption and Scattering of Light by Small Particles*. John Wiley & Sons, New York, 2008.

[24] J. D. Jackson. *Classical Electrodynamics*, volume 3. Wiley, New York, 1962.

[25] E. S. Fry and G. W. Kattawar. Relationships between elements of the stokes matrix. *Appl. Opt.*, 20(16):2811–2814, 1981.

[26] W. J. Wiscombe. Improved mie scattering algorithms. *Appl. Opt.*, 19(9):1505–1509, 1980.

[27] S. Asano and G. Yamamoto. Light scattering by a spheroidal particle. *Appl. Opt.*, 14(1):29–49, 1975.

[28] S. Asano. Light scattering properties of spheroidal particles. *Appl. Opt.*, 18(5):712–723, 1979.

[29] K. S. Yee. Numerical solution of initial boundary value problems involving maxwells equations in isotropic media. *IEEE Trans. Antennas Propag*, 14(3):302–307, 1966.

[30] A. Taflove. *Computational Electrodynamics*. Artech House, Boston, 2000.

[31] E. M. Purcell and C. R. Pennypacker. Scattering and absorption of light by nonspherical dielectric grains. *Astrophys. J.*, 186:705–714, 1973.

[32] Q. H. Liu. The PSTD algorithm: A time-domain method requiring only two cells per wavelength. *Microwave Opt. Technol. Lett.*, 15(3):158–165, 1997.

[33] M. I. Mishchenko. Light scattering by randomly oriented axially symmetric particles. *J. Opt. Soc. Am. A*, 8(6):871–882, 1991.

[34] L. Bi and P. Yang. Accurate simulation of the optical properties of atmospheric ice crystals with the invariant imbedding T-matrix method. *J. Quant. Spectrosc. Radiat. Transfer*, 138:17–35, 2014.

[35] M. I. Mishchenko. Calculation of the amplitude matrix for a nonspherical particle in a fixed orientation. *Appl. Opt.*, 39(6):1026–1031, 2000.

[36] L. Bi, P. Yang, G. W. Kattawar, and M. I. Mishchenko. A numerical combination of extended boundary condition method and invariant imbedding method applied to light scattering by large spheroids and cylinders. *J. Quant. Spectrosc. Radiat. Transfer*, 123:17–22, 2013.

[37] L. Bi and P. Yang. Modeling of light scattering by biconcave and deformed red blood cells with the invariant imbedding T-matrix method. *J. Biomed. Opt.*, 18(5):055001–(1–13), 2013.

[38] P. M. Morse and H. Feshbach. *Methods of Theoretical Physics*. McGraw-Hill, New York, 1953.

[39] L. Tsang, J. A. Kong, and R. T. Shin. *Theory of Microwave Remote Sensing*. John Wiley & Sons, New York, 1985.

[40] L. Tsang, J. A. Kong, K. H. Ding, and C. O. Ao. *Scattering of Electromagnetic Waves, Numerical Simulations*, volume 25. John Wiley & Sons, New York, 2004.

[41] W. H. Press. *Numerical Recipes 3rd Edition: the Art of Scientific Computing.* Cambridge University Press, Cambridge, 2007.

[42] R. Bellman, G. M. Wing, R. E. Bellman, and R. E. Bellman. *An Introduction to Invariant Imbedding.* Wiley, New York, 1975.

[43] S. Asano and M. Sato. Light scattering by randomly oriented spheroidal particles. *Appl. Opt.*, 19(6):962–974, 1980.

[44] P. Yang and K. N. Liou. Finite-difference time domain method for light scattering by small ice crystals in three-dimensional space. *J. Opt. Soc. Am. A*, 13(10):2072–2085, 1996.

[45] B. T. Draine. The discrete-dipole approximation and its application to interstellar graphite grains. *Astrophys. J.*, 333:848–872, 1988.

[46] M. A. Yurkin and A. G. Hoekstra. The discrete dipole approximation: an overview and recent developments. *J. Quant. Spectrosc. Radiat. Transfer*, 106(1):558–589, 2007.

[47] Q. H. Liu. The pseudospectral time-domain (PSTD) algorithm for acoustic waves in absorptive media. *IEEE Trans. Ultrason., Ferroelect. Freq. Contr.*, 45(4):1044–1055, 1998.

[48] G. Chen, P. Yang, and G. W. Kattawar. Application of the pseudospectral time-domain method to the scattering of light by nonspherical particles. *J. Opt. Soc. Am. A*, 25(3):785–790, 2008.

[49] P. Yang and K. N. Liou. Geometric-opticsintegral-equation method for light scattering by nonspherical ice crystals. *Appl. Opt.*, 35(33):6568–6584, 1996.

[50] P. Yang and K. N. Liou. Light scattering by hexagonal ice crystals: solutions by a ray-by-ray integration algorithm. *J. Opt. Soc. Am. A*, 14(9):2278–2289, 1997.

[51] L. Bi, P. Yang, G. W. Kattawar, and R. Kahn. Modeling optical properties of mineral aerosol particles by using nonsymmetric hexahedra. *Appl. Opt.*, 49(3):334–342, 2010.

[52] L. Bi, P. Yang, G. W. Kattawar, Y. Hu, and B. A. Baum. Scattering and absorption of light by ice particles: solution by a new physical-geometric optics hybrid method. *J. Quant. Spectrosc. Radiat. Transfer*, 112(9):1492–1508, 2011.

[53] W. Zheng and S. Ström. The null-field approach to electromagnetic resonance of composite objects. *Comput. Phys. Commun.*, 68(1):157–174, 1991.

[54] S. Strom and W. Zheng. The null field approach to electromagnetic scattering from composite objects. *IEEE Trans. Antennas Propag.*, 36(3):376–383, 1988.

[55] M. I. Mishchenko. Light scattering by size-shape distributions of randomly oriented axially symmetric particles of a size comparable to a wavelength. *Appl. Opt.*, 32(24):4652–4666, 1993.

[56] M. I. Mishchenko and L. D. Travis. T-matrix computations of light scattering by large spheroidal particles. *Opt. Commun.*, 109(1):16–21, 1994.

[57] M. I. Mishchenko, L. D. Travis, and A. Macke. Scattering of light by polydisperse, randomly oriented, finite circular cylinders. *Appl. Opt.*, 35(24):4927–4940, 1996.

[58] D. J. Wielaard, M. I. Mishchenko, A. Macke, and B. E. Carlson. Improved t-matrix computations for large, nonabsorbing and weakly absorbing nonspherical

particles and comparison with geometrical-optics approximation. *Appl. Opt.*, 36(18):4305–4313, 1997.

[59] S. Pulbere and T. Wriedt. Light scattering by cylindrical fibers with high aspect ratio using the null-field method with discrete sources. *Part. Part. Syst. Char.*, 21(3):213–218, 2004.

[60] W. Yan, D. Liu, Y. Du, and H. T. Ewe. Em scattering from multiple cylinders. In *Geoscience and Remote Sensing Symposium, 2009 IEEE International, IGARSS 2009*, volume 2, pages II–730. IEEE, 2009.

[61] B. Friedman and J. Russek. Addition theorems for spherical waves. *Quart. Appl. Math*, 12(13), 1954.

[62] S. Stein. Additional theorems for spherical wave functions. *Q. Appl. Math.*, 19:15–24, 1959.

[63] O. R. Cruzan. Translational addition theorems for spherical vector wave functions. *Quart. Appl. Math*, 20(1):33–40, 1962.

[64] K. A. Fuller and D. W. Mackowski. Electromagnetic scattering by compounded spherical particles. In M. I. Mishchenko, J. W. Hovenier, and L. D. Travis, editors, *Light Scattering by Nonspherical Particles: Theory, Measurements, and Applications*, chapter 8, page 226. Academic Press, San Diego, 2000.

[65] M. I. Mishchenko and L. D. Travis. Capabilities and limitations of a current fortran implementation of the t-matrix method for randomly oriented, rotationally symmetric scatterers. *J. Quant. Spectrosc. Radiat. Transfer*, 60(3):309–324, 1998.

[66] M. A. Yurkin and A. G. Hoekstra. User manual for the discrete dipole approximation code adda v. 0.79. `http://a-dda.googlecode.com/svn/tags/rel_0_`

79/doc/manual.pdf, 2009.

[67] D. W. Mackowski and M. I. Mishchenko. A multiple sphere T-matrix fortran code for use on parallel computer clusters. *J. Quant. Spectrosc. Radiat. Transfer*, 112(13):2182–2192, 2011.

[68] P. W. Barber. Resonance electromagnetic absorption by nonspherical dielectric objects. *IEEE Trans. Microwave Theory Tech.*, 25(5):373–381, 1977.

[69] M. F. Iskander, A. Lakhtakia, and C. H. Durney. A new iterative procedure to solve for scattering and absorption by dielectric objects. *Proc. IEEE*, 70(11):1361–1362, 1982.

[70] M. F. Iskander and A. Lakhtakia. Extension of the iterative ebcm to calculate scattering by low-loss or lossless elongated dielectric objects. *Appl. Opt.*, 23(6):948–953, 1984.

[71] A. Lakhtakia, V. K. Varadan, and V. V. Varadan. Iterative extended boundary condition method for scattering by objects of high aspect ratios. *J. Acoust. Soc. Am.*, 76(3):906–912, 1984.

[72] R. T. Wang and H. C. Van de Hulst. Application of the exact solution for scattering by an infinite cylinder to the estimation of scattering by a finite cylinder. *Appl. Opt.*, 34(15):2811–2821, 1995.

[73] Bruce T Draine and Piotr J Flatau. User guide for the discrete dipole approximation code ddscat 7.3. http://arxiv.org/abs/1305.6497, 2013.

[74] P. C. Waterman and N. E. Pedersen. Electromagnetic scattering by periodic arrays of particles. *J. Appl. Phys.*, 59(8):2609–2618, 1986.

[75] Y. Takano and K. N. Liou. Solar radiative transfer in cirrus clouds. Part I: Single-scattering and optical properties of hexagonal ice crystals. *J. Atmos. Sci.*, 46(1):3–19, 1989.

[76] Q. Cai and K. N. Liou. Polarized light scattering by hexagonal ice crystals: theory. *Appl. Opt.*, 21(19):3569–3580, 1982.

[77] J. M. Sullivan, M. S. Twardowski, P. L. Donaghay, and S. A. Freeman. Use of optical scattering to discriminate particle types in coastal waters. *Appl. Opt.*, 44(9):1667–1680, 2005.

[78] A. L. Alldredge and C. C. Gotschalk. Direct observations of the mass flocculation of diatom blooms: characteristics, settling velocities and formation of diatom aggregates. *Deep Sea Res.*, 36(2):159–171, 1989.

[79] K. A. Fuller and G. W. Kattawar. Consummate solution to the problem of classical electromagnetic scattering by an ensemble of spheres. I: Linear chains. *Opt. Lett.*, 13(2):90–92, 1988.

[80] B. O. Peterson and S. Ström. T-matrix formulation of electromagnetic scattering from multilayered scatterers. *Phys. Rev. D*, 10(8):2670, 1974.

[81] T. Nagumo, K. Osada, and M. Idei. *Diatom World*. National Science Museum, Tokyo, Japan, 2000.

[82] L. Bi, P. Yang, G. W. Kattawar, Y. Hu, and B. A. Baum. Diffraction and external reflection by dielectric faceted particles. *J. Quant. Spectrosc. Radiat. Transfer*, 112(2):163–173, 2011.

[83] W. B. Gordon. Far-field approximations to the kirchoff-helmholtz representations of scattered fields. *IEEE Trans. Antennas Propag.*, 23(4):590–592, 1975.

[84] C. Li, G. W. Kattawar, and P. Yang. Identification of aerosols by their backscattered mueller images. *Opt. Express*, 14(8):3616–3621, 2006.

[85] G. J. Streekstra, A. G. Hoekstra, E. J. Nijhof, and R. M. Heethaar. Light scattering by red blood cells in ektacytometry: Fraunhofer versus anomalous diffraction. *Appl. Opt.*, 32(13):2266–2272, 1993.